

METALLIC GLASS FORMATION AND PROPERTIES IN Zr AND Ti ALLOYED WITH Be—I THE BINARY Zr-Be AND Ti-Be SYSTEMS†

L. E. TANNER

ManLabs, Inc. Cambridge, MA 01239, U.S.A.

and

R. RAY

Department of Chemistry and Materials Science Division, Institute of Chemical Analysis,
Applications and Forensic Science, Northeastern University, Boston, MA 02115, U.S.A.

(Received 9 March 1979; in revised form 16 April 1979)

Abstract—Ultra-rapid liquid-quenching ($> 10^5^\circ\text{C s}^{-1}$) has been found to produce fully glass structures in the binary Zr-Be and Ti-Be alloy systems over composition ranges that bracket the respective eutectics Zr-34.5 at.%Be and Ti-37.5 at.%Be. Both systems also exhibit extended solubility of Be in the Zr and Ti b.c.c. terminal solid solutions. In addition, these studies revealed the existence of metastable ordered phases at 50 at.%Be in the two systems: *m*-ZrBe (orthorhombic B_f , CrB structure type) and *m*-TiBe (cubic B2, CsCl structure type). The experiments clearly indicate that critical cooling rates for glass formation in Ti-Be alloys are significantly higher than in Zr-Be alloys; consequently, only the Zr-Be glasses are readily fabricable in continuous ribbon form. Various criteria for establishing glass forming tendency (GFT) were examined and detailed calculations of critical cooling rates (\dot{T}_c) using the Davies-Uhlmann kinetic formulations were carried out and compared with the experimental results. The composition dependences of certain physical properties of the glasses were also examined and are discussed.

Résumé—Une hypertrempe ($> 10^5^\circ\text{C s}^{-1}$) depuis l'état liquide des alliages binaires Zr-Be et Ti-Be dont la composition entoure respectivement les eutectiques Zr-34,8 at.%Be et Ti-37,5 at.%Be, conduit à une structure entièrement vitreuse. Dans les deux systèmes, on observe une solubilité importante de Be dans les solutions solides terminales c.c. de Zr et Ti. De plus, on a montré l'existence de phases ordonnées métastables à 50 at.%Be, dans les deux systèmes: ZrBe *m* (orthorhombique B_f , structure de type CrB) et TiBe *m* (cubique B2, structure de type CsCl). Les expériences montrent clairement que les vitesses de refroidissement critiques pour la formation de verre sont nettement plus grandes dans les alliages Ti-Be que dans les alliages Zr-Be; par suite, seuls les verres de Zr-Be peuvent être obtenus directement sous la forme de rubans continus. Nous avons examiné divers critères pour la tendance à la formation de verres et calculé en détail les vitesses de refroidissement critiques (\dot{T}_c) à l'aide des formules de Davies et Uhlmann, vitesses que nous avons comparées avec les résultats expérimentaux. Nous avons également étudié et discuté les variations de certaines propriétés physiques des verres en fonction de la composition.

Zusammenfassung—Ultraschnelles ($> 10^5^\circ\text{C s}^{-1}$) Abschrecken aus der Schmelze ergibt vollständige Glasstruktur in den binären Legierungssystemen Zr-Be und Ti-Be über die Zusammensetzungsbereiche, welche die entsprechenden Eutektika Zr-34,8 at.%Be und Ti-37,5 at.%Be erfassen. In beiden Systemen findet man auch eine vergrößerte Löslichkeit von Be in den krz. Zr- und Ti- Endmischkristallen. Dazuhin deckten diese Untersuchungen auch die Existenz metastabiler geordneter Phasen bei 50 at.%Be in beiden Systemen auf: *m*-ZrBe (orthorhombisch B_f , Strukturtyp CrB) und *m*-TiBe (kubisch B2, Strukturtyp CsCl). Die Experimente zeigen deutlich, daß die für Glasbildung kritischen Abkühlgeschwindigkeiten bei den Ti-Be-Legierungen erheblich höher sind als bei den Zr-Be-Legierungen; folglich sind nur die Zr-Be-Gläser leicht als fortlaufende Bänder herstellbar. Es werden verschiedene Kriterien untersucht, die Tendenz zur Glasbildung zu beschreiben, und die kritischen Abkühlgeschwindigkeiten (\dot{T}_c) werden mit der kinetischen Formulierung von Davies-Uhlmann ausführlich berechnet und mit den Messungen verglichen. Die Abhängigkeit gewisser physikalischer Eigenschaften der Gläser von der Zusammensetzung werden ebenfalls untersucht und diskutiert.

1. INTRODUCTION

Recognition of the technological potential of metallic glasses [1, 2] has generated considerable activity in this field in recent years [3-5]. As a consequence,

many new glass-forming alloys have been discovered, the unique properties of certain of these glasses have been systematically optimized and still further, the methods for ultra-rapid liquid-quenching have been advanced so that it is now possible to fabricate rather large quantities of these materials in such useful forms as continuous ribbons and tapes.

The high strength and ductility intrinsic to metallic

† This work was carried out at the Corporate Research Center, Allied Chemical Corporation, Morristown, NJ 07960, U.S.A.

glasses are of particular interest, and the enhancement of mechanical behavior has been given special attention [6]. A principal accomplishment of these efforts has been the development of ultra-high strength, elastically stiff, thermally stable ferrous-based metal/metalloid glasses, e.g. $\text{Fe}_{80}\text{B}_{20}$,[†] METGLAS® 2605 [7, 8]. In the current work, we have gone a step further by developing glasses with high specific strength; that is, synthesizing strong glasses in alloys containing low-density elements.

A wide variety of binary alloys were screened for glass formability by means of splat-quenching. Each alloy system comprised of at least one low-density element, was characterized by one or more well-defined eutectic reactions (where eutectic temperatures, T_e , were $>700^\circ\text{C}$). Primary focus was on the compositions at, or near, the eutectics since metallic glasses almost invariably form within these reduced melting regions [9]. The lower limit on melting temperature was imposed to ensure that any resulting glasses would be stable well above room temperature, since experience has shown that devitrification proceeds rapidly at $0.4\text{--}0.6 T_e$ [3–5].

This initial search revealed glass formation in Ti-Be and Zr-Be alloys, among others. Optimization of strength, density, thermal stability and ease of ribbon fabrication accomplished by means of composition variation led to the ternary formulation

$\text{Ti}_{50}\text{Be}_{40}\text{Zr}_{10}$ (METGLAS® 2204) [11]. Its yield strength (σ_y) is ~ 2.27 GPa and its density (ρ) is $4.13 \times 10^3 \text{ kg m}^{-3}$; hence, the specific strength ($\sigma_y \rho^{-1}$) of $\text{Ti}_{50}\text{Be}_{40}\text{Zr}_{10}$ is $56 \times 10^3 \text{ m}$, which is the highest value attained thus far for a metallic glass in ductile ribbon form [11].[‡]

In the course of this development program, the glass-forming behavior and attendant physical properties of the Zr-Be, Ti-Be and Zr-Ti-Be systems were examined in detail. Formation behavior and the variations in hardness, density and thermal stability as functions of composition in the binary alloy glasses are reported here. The results pertaining to the ternary glasses will be presented in Part II [12].

2. EXPERIMENTAL

Alloys were prepared from high purity materials by means of arc-melting in an inert atmosphere of purified argon. The compositions were $\text{Zr}_{(100-x)}\text{Be}_x$ and $\text{Ti}_{(100-x)}\text{Be}_x$, where x ranged from 2.5 to 70 at.%. These alloys were initially liquid-quenched by the arc-splat/hammer-and-anvil technique [13], where foil thickness varied from $<0.3 \mu\text{m}$ to $30 \mu\text{m}$. Subsequently, glass-forming compositions were fabricated into continuous ribbons of $10\text{--}30 \mu\text{m}$ thickness and $1\text{--}2 \text{ mm}$ width [14]. Only the Zr-Be alloys could be produced as ribbons having a completely glassy structure. Structure was primarily determined by means of X-ray diffraction (XRD) using filtered $\text{CuK}\alpha$ and $\text{MoK}\alpha$ radiation. Selected samples were also examined by transmission electron microscopy (TEM)

[†] Subscripts are in atomic per cent.

[‡] In our most recent work we have synthesized metallic glass ribbons of $\text{Ti}_{60}\text{Be}_{35}\text{Si}_5$ with a specific strength of $65 \times 10^3 \text{ m}$ [see *Scripta metall.* 12, 703 (1978).]

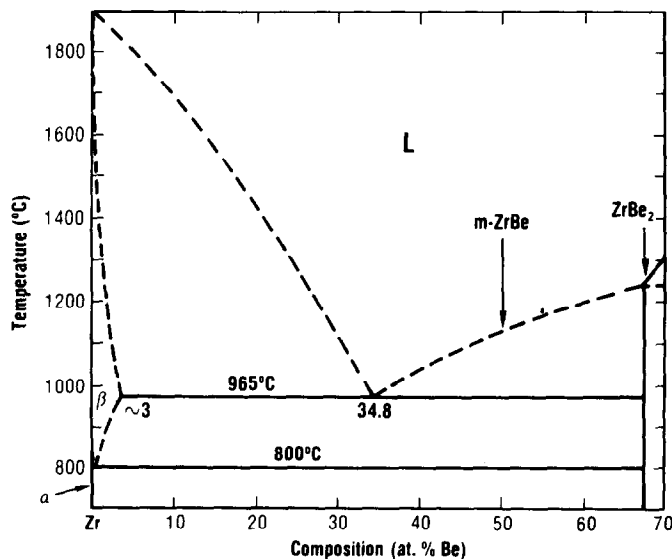


Fig. 1(a).

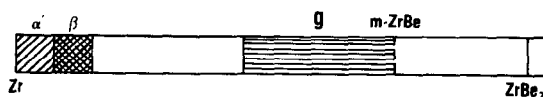


Fig. 1(b).

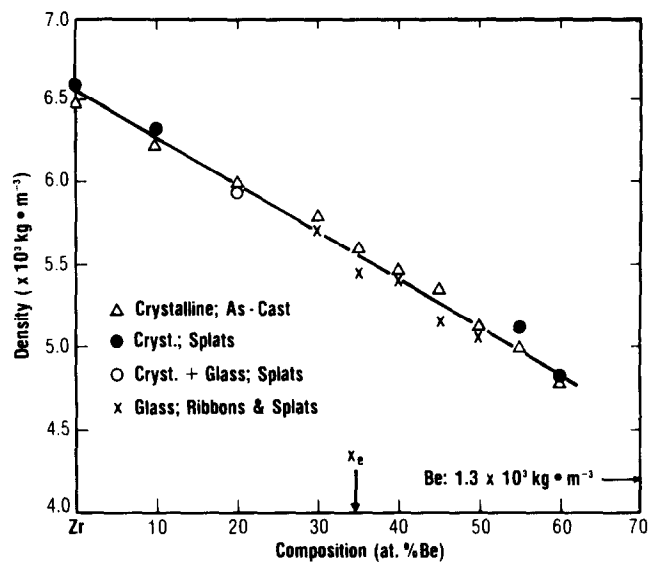


Fig. 1(c).

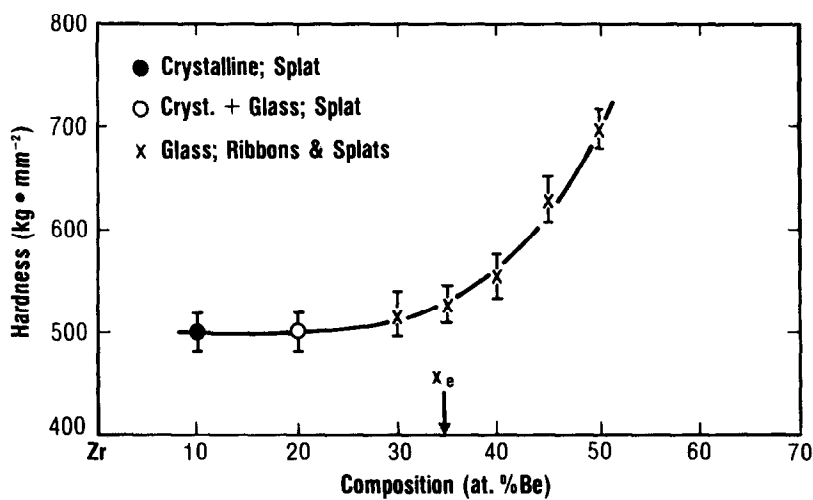


Fig. 1(d).

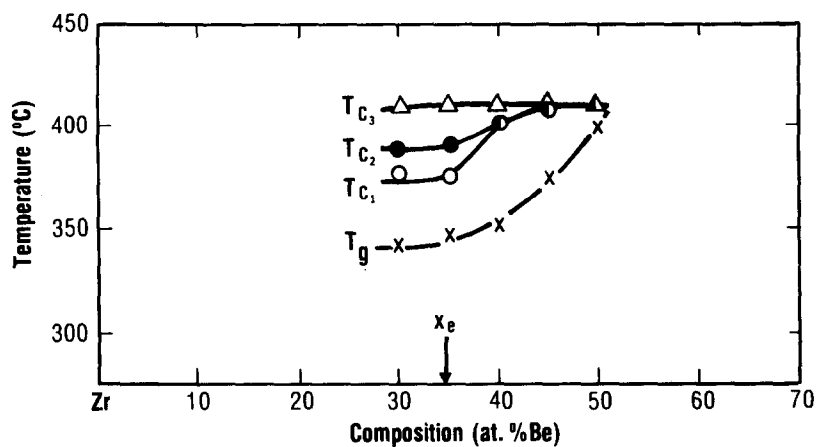


Fig. 1(e).

Fig. 1. The Zr-Be system. (a) Partial equilibrium phase diagram from Ref. [16]; also indicating meta-stable ordered phase $m\text{-ZrBe}$. (b) Quenched-phase plot for ultra-rapid liquid cooling giving maximum extent of supersaturation, glass formation, and positions of stable and metastable phases. (c) Density vs composition for stable and metastable phases. (d) Hardness vs composition for glass, crystalline, and glass + crystalline structures. (e) Transformation temperatures vs composition for glassy ribbons heated in DSC at $20^{\circ}\text{C min}^{-1}$ (see text for details).

using a JEM 200 instrument. Specimen regions that were not electron transparent (viz., $>0.3 \mu\text{m}$) were electrothinned by the method described by Spurling [15] using an electrolyte of 5% H_2SO_4 (by volume) in methanol, cooled to about -50°C .

The Vicker's diamond pyramid microhardness H_v was measured on epoxy mounted and polished samples using a Leitz Miniload instrument with 50 and 100 g loads. Values of H_v are accurate to $\pm 5\%$.

The glass-to-liquid transition and the sequence of devitrification processes were examined by differential scanning calorimetry (DSC), up to $\sim 700^\circ\text{C}$, during continuous heating in argon at $20^\circ\text{C min}^{-1}$ using a Perkin-Elmer DSC-2 unit. Selected specimens were studied to higher temperatures by differential thermal analysis (DTA) in helium at a heating rate of $15^\circ\text{C min}^{-1}$ in a Mettler TA-1 instrument.

Density, ρ , was determined by comparing specimen weight in air and in a liquid of known density at room temperature with an accuracy of $\pm 0.5\%$.

3. RESULTS

3.1 The Zr-Be system

The partial equilibrium phase diagram is presented in Fig. 1(a) [16]. Figure 1(b) is a quenched-phase plot (for maximum cooling rate) showing a glass formation range from 30 to 50 at.% Be. Table 1 summarizes the structures observed in each of the rapidly cooled alloys. Figures 1(c-e) describe the composition dependences of density, hardness and the glass transition

and crystallization temperatures, T_g and T_c , respectively.

Be solubility in the low-temperature solid solution α (A3, h.c.p.) is <1 at.%, while the high-temperature phase β (A2, b.c.c.) is reported to dissolve a maximum of ~ 3 at.% at the eutectic temperature 965°C [16]. Liquid-quenched splat foils with up to 5 at.% Be are single phase h.c.p. TEM examination shows the microstructure to be acicular martensite, α' , which forms from β during cooling [17]. Figure 2(a) shows an apparently continuous and uniform distribution of fine α' platelets in the 2.5 at.% Be alloy. The 5 at.% alloy [Fig. 2(b)] contains still finer α' within equiaxed regions of $\sim 1 \mu\text{m}$ average diameter which define the original β grain structure. In the 7.5 at.% alloy [Fig. 2(c)], α' and retained β are easily identified, while both electron and X-ray diffraction also indicate the presence of the glassy phase and ZrBe_2 . The 10 at.% Be sample comprises primarily retained β and the glass. In Fig. 2(d) we see rosettes which developed from spherical β centers of $\sim 0.5 \mu\text{m}$ dia. embedded in a glassy matrix; the α' and equilibrium ZrBe_2 are located at the outer extremities of the rosettes, i.e. within the dendritic regions. The 15-25 at.% Be samples showed similar structures, where thinner (electron transparent) regions contained fewer rosettes, but in no instance was there evidence of a uniform fine-grained structure of single-phase retained β . The fully glass structure of $\text{Zr}_{70}\text{Be}_{30}$ ribbon is shown in Fig. 2(e). In addition to the phases mentioned, some splat-foils of the 15, 50, 55 and 60 at.% Be alloys

Table 1. Room-temperature composition and constitution of liquid-quenched Zr-Be alloys

Alloy Composition (at.% Be)	Glass	Crystalline Phases					
		α' (a)		β (b)		$m - \text{ZrBe}$ (c)	ZrBe_2 (d)
		\bar{V} ($\times 10^3 \text{ nm}^3$)	$x^{(e)}$ (at.% Be)	\bar{V} ($\times 10^3 \text{ nm}^3$)	$x^{(e)}$ (at.% Be)	\bar{V} ($\times 10^3 \text{ nm}^3$)	\bar{V} ($\times 10^3 \text{ nm}^3$)
2.5	—	23.00	2.5	—	—	—	—
5	—	22.71	5	—	—	—	—
7.5	x	22.70	5	22.60	7.5	—	13.57
10	x	22.75	5	22.40	10	—	13.57
15	x	22.70	5	22.40	10	15.92	13.57
20 ^(g)	x	—	—	22.38	10	—	—
25 ^(g)	x	—	—	22.39	10	—	—
30-45 ^(g)	x	—	—	—	—	—	—
50	x	—	—	—	—	—	—
55	x	23.27	<1	—	—	15.92	13.57
60	x	23.27	<1	—	—	15.92	13.57
65	x	(f)	(?)	—	—	—	13.57
67	x	—	—	—	—	—	13.57

(a) Supersaturated A3 (h.c.p.) solid solution produced by martensitic transformation of high-temperature β phase. The low-temperature equilibrium α is also h.c.p.; room-temperature composition is <1 at.% Be; $a_0 = 0.321 \text{ nm}$, $c_0 = 0.5148 \text{ nm}$, $\bar{V} = 23.272 \times 10^3 \text{ nm}^3$.

(d) Stable ordered phase C32 (hexagonal, AlB_2 -type), $a_0 = 0.381 \text{ nm}$, $c_0 = 0.323 \text{ nm}$ and $\bar{V} = 13.570 \times 10^3 \text{ nm}^3$.

(c) Metastable ordered phase B_r (orthorhombic, CrB-type), $a_0 \approx 0.336 \text{ nm}$, $b_0 \approx 1.028 \text{ nm}$, $c_0 \approx 0.369 \text{ nm}$ and $\bar{V} \approx 15.92 \times 10^3 \text{ nm}^3$.

(d) Stable ordered phase C32 (hexagonal, AlB_2 -type), $a_0 = 0.381 \text{ nm}$, $c_0 = 0.323 \text{ nm}$ and $\bar{V} = 13.570 \times 10^3 \text{ nm}^3$.

(e) Estimated solute supersaturation (see text).

(f) α' observed, but diffraction peaks too weak to obtain lattice parameters.

(g) Ribbons, as well as splat-foils.

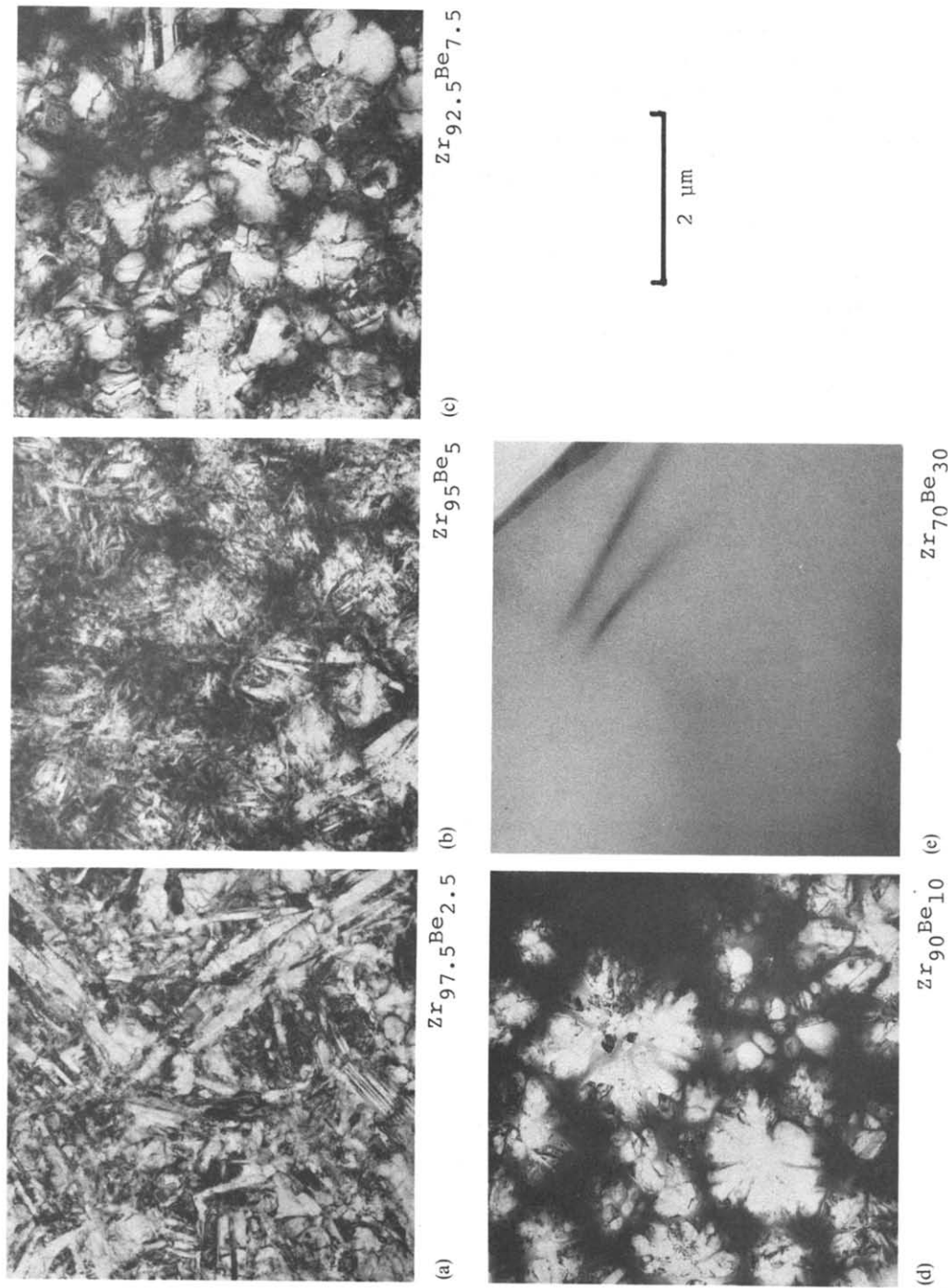


Fig. 2. Transmission electron micrographs (bright field) of rapidly quenched Zr-Be alloys. (a) 2.5 at.% Be, acicular martensite, single phase α' . (b) 5 at.% Be, same as in (a) but showing original spherical shape of primary β formed from the liquid. (c) 7.5 at.% Be, α' plus retained β and ZrBe₂. (d) 10 at.% Be, multiphase rosettes in a glassy matrix, where centers are predendritic β spheres (see text). (e) 30 at.% Be, fully glass structure.

revealed a number of weak, unknown peaks in XRD patterns. These were subsequently associated with the B_f (CrB-type) structure [18], viz. a metastable ordered phase (MOP) [19] designated m -ZrBe. Identification followed the discovery of an isomorphous MOP in liquid-quenched Hf-Be and Hf-Zr-Be alloys [20]. Approximate lattice parameters for the B_f orthorhombic cell of m -ZrBe are $a_0 \approx 0.336$ nm, $b_0 \approx 1.028$ nm and $c_0 \approx 0.369$ nm.

A plot of mean atomic volume (\bar{V}) vs Be concentration (x) in Fig. 3 shows that the stable Zr-Be phases [18], as well as m -ZrBe, obey Vegard's law [21] rather closely. Using the lattice parameters observed for α' , we see that $\bar{V}^{\alpha'}$ (also plotted in Fig. 3) exhibits a small positive deviation from Vegard's law; it then remains essentially constant for $5 \leq x \leq 15$. Metastable β is retained in alloys of 7.5 to 25 at.%Be, but is always found in the presence of other phases. Maximum supersaturation in β was estimated to be ~ 10 at.%Be; the reasoning for this conclusion will be discussed in Section 4.1.1.

The densities of metallic glasses are typically within 1–2% of those of the corresponding crystalline state [22, 23]. This is confirmed in the plot given in Fig. 1(c).

Figure 1(d) shows that hardness of the glasses increases from 500 kg mm^{-2} at 30 at.%Be to 700 kg mm^{-2} at 50 at.%Be, with the curve exhibiting a positive deviation from linearity.

DSC traces for heating the as-quenched glasses display the endothermic and exothermic effects associated with the sequence of transitions from the glass-to-supercooled liquid-to-polycrystalline, multiphase

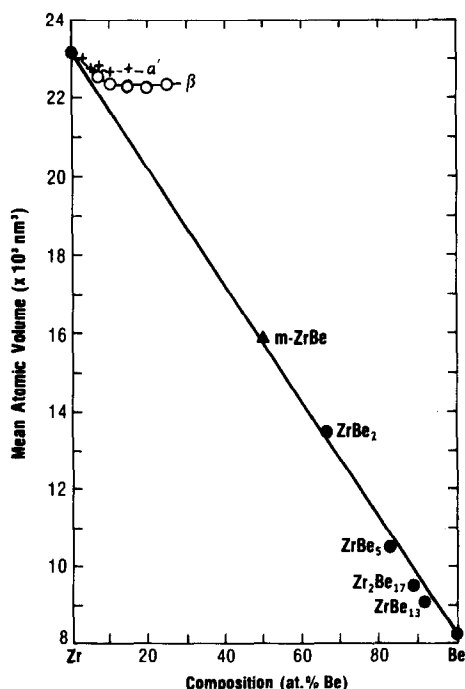


Fig. 3. Mean atomic volumes \bar{V} of stable Zr-Be phases and metastable phases m -ZrBe, supersaturated β and α' .

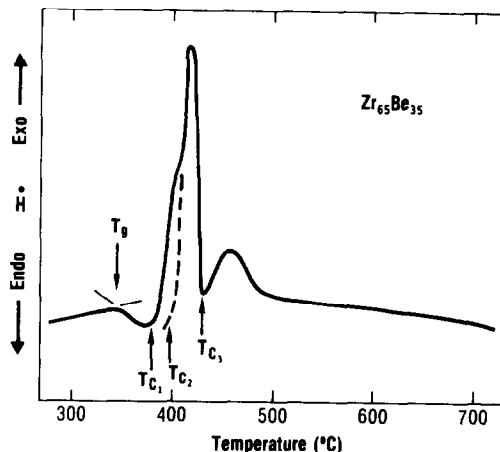


Fig. 4. DSC thermogram of eutectic composition $\text{Zr}_{65}\text{Be}_{35}$ glass obtained by heating at $20^\circ\text{C min}^{-1}$. The glass transition T_g and crystallization temperatures T_c are indicated; see Fig. 1(e) for data from other compositions. Final microstructure is equilibrium $\alpha + \text{ZrBe}_2$.

aggregates. Each stage was examined individually by rapidly cooling samples from temperatures, during and following the completion of a transition, and then using XRD to identify the resulting structures. The first effect observed is endothermic arising from the rapid rise in specific heat (C_p) at the glass \rightarrow liquid transition [24]. The onset of the increase is designated the glass transition temperature (T_g) as indicated on the thermogram for $\text{Zr}_{65}\text{Be}_{35}$ in Fig. 4. Samples cycled through T_g , but cooled prior to reaching the exotherms at higher temperatures, maintain the broad-peak XRD pattern characteristic of a wholly glassy structure [25]. It was noted that repeated cycles result in a generalized exothermic effect over the entire span of temperature (e.g. see Fig. 1(b), Ref. [11]); this is the thermal manifestation of relaxation of the as-quenched glass to lower energy atomic configurations approaching the ideal glass state [26, 27]. Further heating of the $\text{Zr}_{65}\text{Be}_{35}$ glass produces two exotherms; the first comprises two narrow, overlapping peaks and the second is a single broad peak (Fig. 4). Interrupting the first reaction at successively higher temperatures revealed that T_{c1} is associated with the formation of equilibrium (Be-lean) α , and T_{c2} (hidden within the exotherm) is the start of the precipitation of ZrBe_2 . The separation of these reactions is much more apparent at lower Be contents [see Fig. 1(e)]. XRD at the end of this stage shows that some glassy phase still remains. Complete transformation (and, perhaps, some form of recrystallization and/or phase coarsening as revealed by diffraction peak sharpening) initiates at T_{c3} . Figure 1(e) shows that T_{c3} remains roughly constant with varying x , while T_{c1} ($+T_{c2}$) rise sharply with increasing Be, so that all the reactions tend to merge in hypereutectic alloys. A detailed XRD examination of the alloy structures did not reveal the formation of the MOP m -ZrBe. Hence, this phase does not appear to take the role of an intermediate transformation product

here, as does its counterpart m -HfBe during the devitrification of Hf-Be glasses [20], or as m -TiBe does in the devitrification Ti-Be of glasses (the latter will be discussed in Section 3.2). It is important to emphasize at this point that XRD can only provide an overall description of structural changes, but cannot elucidate either the mode(s) or morphology of the reactions. TEM is required to examine the micro-morphology at each stage and this was beyond the scope of the current study.

Figure 1(e) also contains a plot of T_g vs x . Note the similarity of curvature to that of the variation of H_v with x , cf. Fig. 1(d).

The heating of supersaturated crystalline and partially crystalline samples in the DSC exhibit expected thermal effects up to 730°C and, in all cases, the final reaction products are equilibrium α -Zr + ZrBe₂. Some of the glasses were heated to $T > 730^\circ\text{C}$ in the DTA unit and this revealed the $\alpha \rightleftharpoons \beta$ allotropic transformation sharply at 800°C upon heating (endothermic) and upon cooling (exothermic).

3.2 The Ti-Be system

The partial binary phase diagram [28, 29], given in Fig. 5(a), is seen to be rather similar to that of Zr-Be [cf. Fig. 1(a)]. However, we found that rapidly cooled Ti-Be alloys can exhibit significantly different behavior. Figure 5(b) is the quenched-phase plot which shows the glass-forming range to be quite restricted and also indicates the unambiguous presence of the MOP m -TiBe. Table 2 summarizes the as-quenched structures and other data pertaining to the stable and metastable phases. Fully glass, but extremely thin ($< 10\ \mu\text{m}$), foils were consistently produced by splat-quenching between 37–41 at.%Be, and only intermittently in alloys up to 45 at.%Be. Also, as noted earlier,

attempts to fabricate completely glassy ribbons were unsuccessful; this firmly establishes that the Ti-Be alloys require distinctly higher cooling rates for glass formation than are required for the Zr-Be alloy glasses, and that these rates approach the maximum currently attainable in the laboratory [9, 30–32].

As with the Zr-Be system, the equilibrium α terminal solid solution allows for little or no solubility of Be [28, 33]. The high-temperature β phase has a maximum solubility of ~ 5 at.%Be and transforms martensitically to α' during normal water-quenching of bulk solid specimens [29]. Splat-quenching the Ti₉₅Be₅ liquid produces single phase α' identical to that found in Zr_{97.5}Be_{2.5} [see Fig. 2(a)]. The microstructural features of higher Be contents are also comparable to those described in the remainder of Fig. 2. As in the Zr-Be system, the alloys on either side of the glass region are multiphase aggregates. Untransformed (apparently) supersaturated β appears in alloys $7.5 < x < 30$ at.%Be; the other phases are the glass, m -TiBe and/or TiBe₂ (see Table 2). At $x > 30$, m -TiBe is the major phase and α' (or α) shows little or no supersaturation. Hence, m -TiBe appears to replace β as the primary nucleant from the liquid and this was tentatively confirmed by TEM. A plot of \bar{V} vs x in Fig. 6 indicates that the equilibrium Ti-Be phases [18] exhibit a rather small negative deviation from Vegard's law. This plot includes \bar{V} for the MOP m -TiBe which was identified as a B2 (CsCl-type) cubic structure [33].

Table 2 gives the atomic volumes for single phase α' calculated from observed lattice parameters. Values of $\bar{V}^{\alpha'}$ plotted in Fig. 6 indicate a small positive deviation from Vegard's law; $\bar{V}^{\alpha'}$ remains essentially constant at $\sim 17.35 \times 10^{-3}\ \text{nm}^3$ for $5 < x < 30$ indicating that 5 at.%Be is the approximate limit of instability

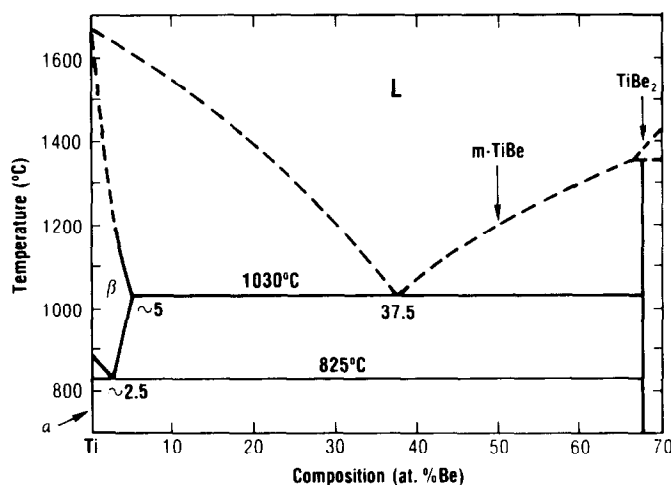


Fig. 5(a).

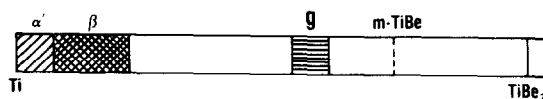


Fig. 5(b).

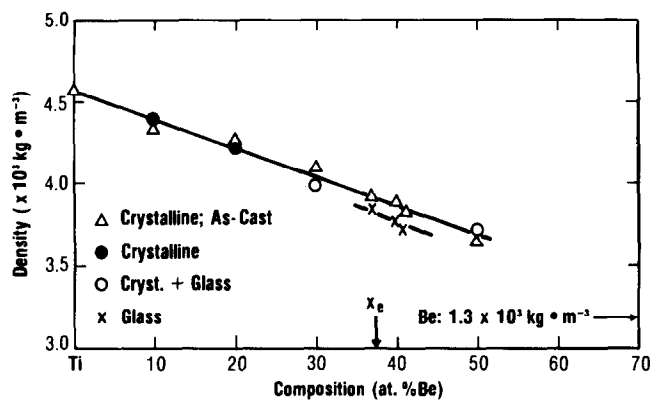


Fig. 5(c).

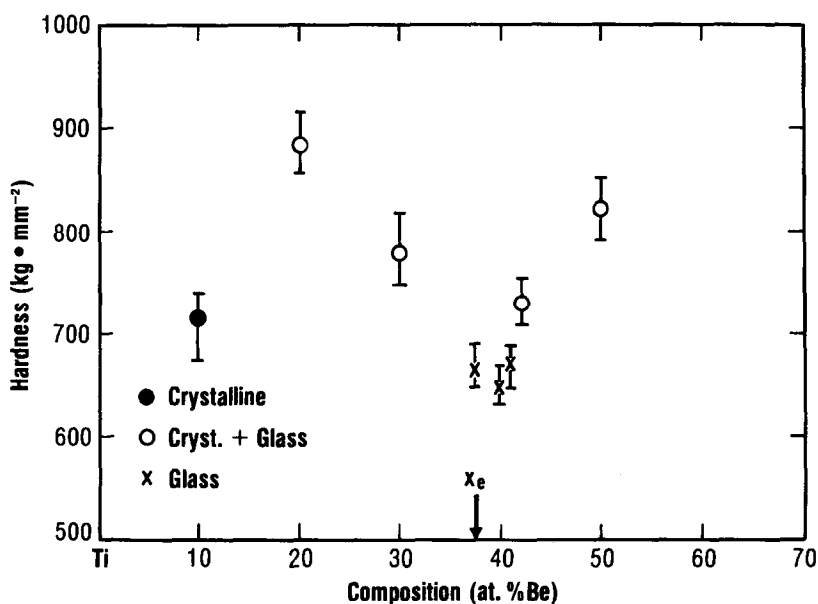


Fig. 5(d).

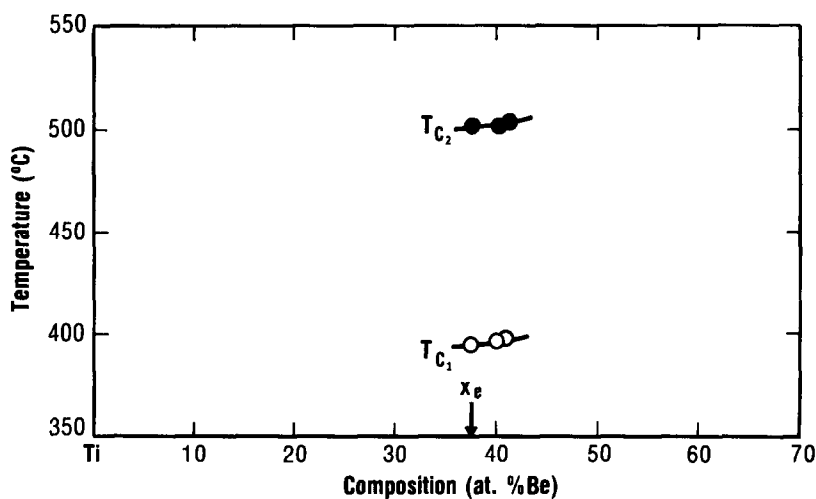


Fig. 5(e).

Fig. 5. The Ti-Be system. (a) Partial equilibrium phase diagram from Refs. [28] and [29]; also indicating metastable ordered phase *m*-TiBe. (b) Quenched phase plot for ultra-rapid liquid cooling giving maximum extent of supersaturation, glass formation, and positions of stable and metastable phases. (c) Density vs composition for stable and metastable phases. (d) Hardness vs composition for glass, crystalline, and glass + crystalline structures. (e) Transformation temperatures vs composition for glassy splat-foils heated in DSC at $20^{\circ}\text{C min}^{-1}$ (see text for details).

Table 2. Room-temperature composition and constitution of liquid-quenched Ti-Be alloys

Alloy Composition (at. % Be)	Glass	Crystalline Phases					
		α (a)		β (b)		m -TiBe (c)	TiBe ₂ (d)
		\bar{V} ($\times 10^3$ nm ³)	x (e) (at. % Be)	\bar{V} ($\times 10^3$ nm ³)	x (e) (at. % Be)	\bar{V} ($\times 10^3$ nm ³)	\bar{V} ($\times 10^3$ nm ³)
2.5	—	17.50	2.5	—	—	—	—
5	—	17.35	5	—	—	—	—
7.5	—	17.35	5	17.05	7.5	12.72	—
10	—	17.36	5	16.72	10	12.72	—
15	x	17.35	5	16.56	15	12.72	11.129
20	x	(f)	(?)	16.55	15	12.72	—
25	x	—	—	16.63	15	12.72	—
30	x	—	—	16.54	15	12.72	—
35	x	—	—	16.56	15	12.72	—
37-41	x	—	—	—	—	—	—
42	x	(f)	(?)	17.03	6-8	12.72	11.129
43	x	17.55	< 1	—	—	12.72	11.129
44	x	(f)	(?)	17.11	6-8	12.72	11.129
45	x	(f)	(?)	—	—	12.72	11.129
50	x	17.56	< 1	—	—	12.72	11.129
55	—	—	—	—	—	—	11.129
60	—	—	—	—	—	—	11.129
67	—	—	—	—	—	—	11.129

(a) Supersaturated A3 (h.c.p.) solid solution produced by martensitic transformation of high-temperature β phase. The low-temperature equilibrium α is also h.c.p.; room-temperature composition is $\ll 1$ at.%Be; $a_0 = 0.2945$ nm, $c_0 = 0.4675$ nm and $\bar{V} = 17.557 \times 10^3$ nm³.

(b) High-temperature solid solution A2 (h.c.c.), maximum equilibrium composition ~ 5 at.%Be at 1030°C.

(c) Metastable ordered phase B2 (cubic, CsCl-type), $a_0 = 0.294$ nm and $\bar{V} = 12.72 \times 10^3$ nm³.

(d) Stable ordered phase C15 (cubic, MgCu₂-type), $a_0 = 0.644$ nm and $\bar{V} = 11.129 \times 10^3$ nm³.

(e) Estimated solute supersaturation (see text).

(f) α' observed, but diffraction peaks too weak to obtain lattice parameters.

of b.c.c. β . Untransformed β , retained (in the company of other phases) in alloys of higher Be content suggest that its maximum supersaturation is ~ 15 at.% (see Table 2); this will be discussed in Section 4.1.1.

The densities of the crystalline and glassy alloys are plotted in Fig. 5(c). The glasses are 1-2% less dense than their crystalline counterparts [22, 23].

The hardnesses of glasses in the 37-41 at.%Be range are 650-670 kg mm⁻² [Fig. 5(d)]. The erratic values for the crystalline and partially crystalline samples could be related to rather non-uniform distributions

of the relatively harder phases m -TiBe and TiBe₂, and this was confirmed by quantitative XRD.

The DSC traces on heating these glasses do not show a glass transition, though one is observed at $\sim 400^\circ\text{C}$ in the ternary Ti₅₈Be₄₀Zr₂ [12]. Figure 7(a) is a thermogram for Ti₆₃Be₃₇ and the two exotherms observed are related to two independent crystallization reactions; T_{c1} and T_{c2} as a function of x are plotted in Fig. 5(e). In the first reaction, the as-quenched glass (g) transforms to equilibrium (Be-lean) α plus a Be-enriched glass (g'). The higher temperature reaction completes crystallization, viz. $\alpha + g' \rightarrow \alpha + m$ -TiBe. The MOP m -TiBe is also found in ternary alloys, substituting Zr for Ti [11, 12, 33], and the kinetics of isothermal crystallization have been measured for the Ti₅₀Be₄₀Zr₁₀ glass [11].

Figure 7(b) shows a DTA thermogram for a Ti₅₆Be₄₄ glass (heated at $15^\circ\text{C min}^{-1}$ to 1003°C , i.e. just below the initiation of melting) which exhibits the same low-temperature effects described above, and then reveals a broad complex, primarily endothermic, reaction starting at $\sim 825^\circ\text{C}$. A narrow exotherm appears at this temperature during cooling at the same rate, but no other effects are observed at lower temperatures since complete crystallization occurred during the initial heating. Subsequent cycles reveal only the narrow endotherm (heating) and exotherm (cooling) at 825°C . XRD of the sample following the first and second cycles showed the presence of equilibrium $\alpha + \text{TiBe}_2$, plus a new series of diffraction peaks, while the m -TiBe spectrum was now missing. It is important to note that m -TiBe remains

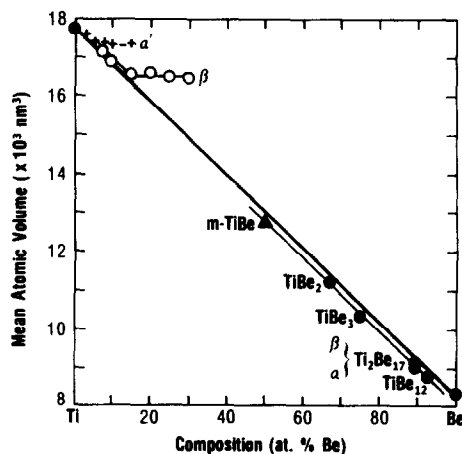
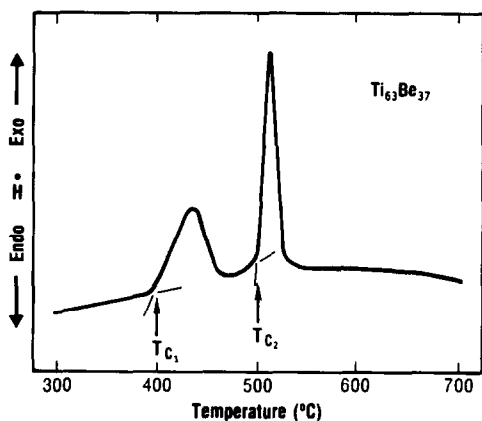


Fig. 6. Mean atomic volumes \bar{V} of stable Ti-Be phases and metastable phases m -TiBe and supersaturated β and α' .

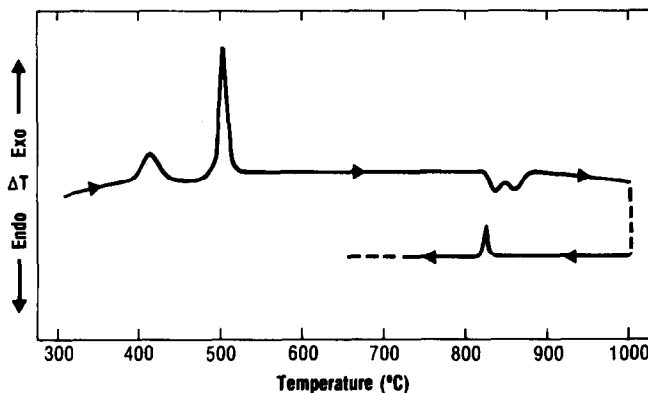
stable in all the DSC cycles up to the maximum temperature of the DSC-2 instrument (viz. 730°C).

The heating endotherms and cooling exotherms at 825°C are manifestations of the $\alpha \rightleftharpoons \beta$ transformation as described earlier for Zr-Be alloys. However, the complexity in the initial cycle may also be related to a concurrent reversion of metastable *m*-TiBe and the formation of stable TiBe₂. In addition, we must account for the presence of a new phase. The extra diffraction peaks have been indexed as a cubic η phase (E9₃, Fe₃W₃C-type) [34] which is believed to be of Ti₃Be₃(O, N)_x stoichiometry (where 0.5 < *x* < 1.0) having a lattice parameter of *a*₀ = 1.0712 nm [35]. Its origin will be discussed later.

Finally, unlike Zr-Be alloys, heating the metastable crystalline and partially crystalline splat-foils to 730°C does not completely revert the microstructures to their equilibrium state. The α' rejects its excess Be (becoming effectively α -Ti), β phase disappears and some TiBe₂ is precipitated, but *m*-TiBe resists reversion up to this temperature.



(a)



(b)

Fig. 7. Thermograms for Ti-Be glassy splat-foils. (a) DSC trace of eutectic composition Ti₆₃Be₃₇ heated at 20°C min⁻¹ showing crystallization temperatures *T*_{c1} and *T*_{c2}; resultant structure: equilibrium, α -Ti plus metastable *m*-TiBe; see Fig. 5(e) for data from other compositions. (b) DTA trace of Ti₅₆Be₄₄ for heating and cooling at 15°C min⁻¹. Maximum temperature is 1003°C, just below melting; resultant structure: equilibrium α , TiBe₂ plus η phase (see text for details).

4. DISCUSSION

The phase relations observed in rapidly cooled alloys can be conveniently summarized in a form of non-equilibrium phase diagram in which cooling rate, \dot{T} , is plotted against composition, *x* [36]. The relationships between \dot{T} , the heat transfer rate from the liquid to the solid substrate, and the final quenched sample thickness, *d*, have been examined in some detail [37, 38]. Comparisons with experiments made by Jones [38] lead to the conclusion that both splat and ribbon formation are best approximated by intermediate cooling conditions. Intermediate rates fall between *ideal* cooling conditions, where the interface provides no barrier to thermal conduction (here $\dot{T} \sim d^{-2}$) and *Newtonian* cooling conditions, where heat transfer is relatively poor and hence cooling is interface controlled (in this case $\dot{T} \sim d^{-1}$). Judging \dot{T} from observed values of *d*, and associated variations of quenched-in microstructure, with *x*, we can estimate the position of boundaries between the crystalline and glassy states in \dot{T} vs *x* diagrams; the results for the Zr-Be and Ti-Be systems are plotted in Figs. 8 and 9, respectively. The upper limit of \dot{T} for arc-splating is of the order of 10⁹ K s⁻¹ (*d* < 1 μ m), whereas for ribbon formation, \dot{T}_{max} may approach 10^{7.5} K s⁻¹ (*d* < 5–10 μ m), but on average, \dot{T} is 10⁶–10⁷ K s⁻¹ (for ribbon *d* in the range 20–40 μ m).

Following Giessen *et al.* [30, 31] among others, we can analyze these results by initially examining the constitutional conditions for stable and metastable states and their dependences on \dot{T} (or alternatively, the degree of undercooling). Subsequent modifications may be derived from consideration of transformation kinetics parameters, as well as other, perhaps less important factors.

4.1 Metastable crystalline states

4.1.1. *Terminal solid solutions.* Hypoeutectic alloys in both systems form the β phase from the melt most

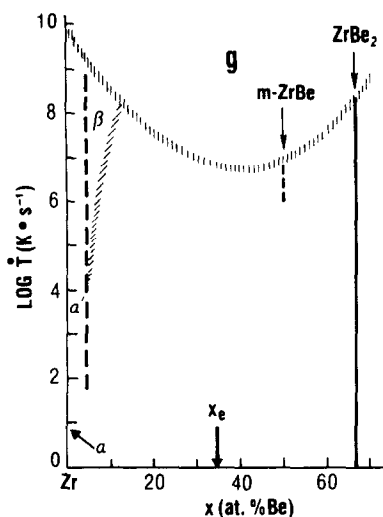


Fig. 8. Cooling rate (\dot{T}) vs composition for liquid-quenching of Zr-Be alloys.

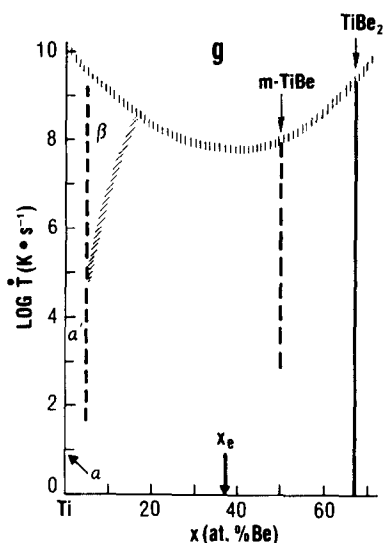


Fig. 9. Cooling rate (\dot{T}) vs composition for liquid-quenching of Ti-Be alloys.

readily, particularly as Be content decreases. In low Be alloys, experimental observations indicate that the martensite start (M_s) and finish (M_f) temperatures cannot be bypassed by these ultra-rapid quenches; hence, the primary β transforms to α' (without further decomposition), thus producing supersaturated h.c.p. solid solutions [39]. In Zr-Be, the Be content in α' reaches 5 at.% which exceeds the maximum equilibrium solubility in β (cf. Figs. 1, 3 and Table 1). The solubility in primary β is increased from 3 to about 10 at.%Be as indicated by microstructure and diffraction evidence. The original β grains in the 5 and 7.5 at.% alloys appear to have been spherical in shape [see Figs. 2(b) and (c), respectively]. The retained β centers of the rosettes observed in the 10 at.% alloy are also spherical [Fig. 2(d)]. This is indicative of β forming by 'diffusionless' solidification, i.e. β maintains the liquid composition during nucleation and

(early) growth. The rosette centers are comparable to the 'predendrites' observed by Biloni and Chalmers [40] in chill-cast Al-Cu ingots, and by Ramachandrarao *et al.* [41] in Al-Ge splat-foils. Such behavior can be understood by referring to a portion of a typical eutectic phase diagram of solvent A and solute B in Fig. 10(a), and the corresponding schematic representation of free energy curves in Fig. 10(b) [30]. The relative positions of the free energies G_L of the liquid (for three successively lower temperatures) are shown with respect to the curves G_S for the terminal solid solution, where the latter are assumed to be temperature independent. G_S^I represents a weak and G_S^{II} a strong, positive deviation from Raoult's law [42]. The maximum equilibrium solubility of B in A at T_1 is S_1 (by the tangent rule), while the maximum metastable supersaturation corresponds to the crossover of G_S and G_L at C_1 . This can be carried out for increasing undercoolings ($T \rightarrow T_1, T_2, T_3 \dots T_i$) giving rise to the T_0 curves (the loci of $C_1, C_2, C_3 \dots C_i$) in Fig. 10(a). It is seen that alloys with compositions $x < C_i$ can decrease their free energies by initially solidifying without rejecting solute, i.e. in a 'predendritic/diffusionless' manner [40]. This is obviously not the maximum reduction in G between C_i and S_1 , but is likely to be the kinetically favored path when heat is being very rapidly extracted from the melt as in splat-quenching. For $x > C_i$ the liquid is constrained to transform into multiphase structures requiring

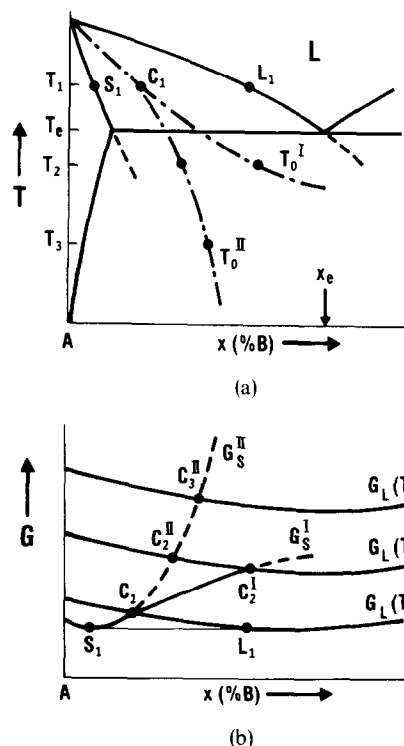


Fig. 10. Hypothetical eutectic binary system. (a) Phase diagram indicating role of parameter T_0 . (b) Free energy diagram for a series of temperatures and two solid solutions with differing positive deviations from Raoult's law. (From Ref. [30].)

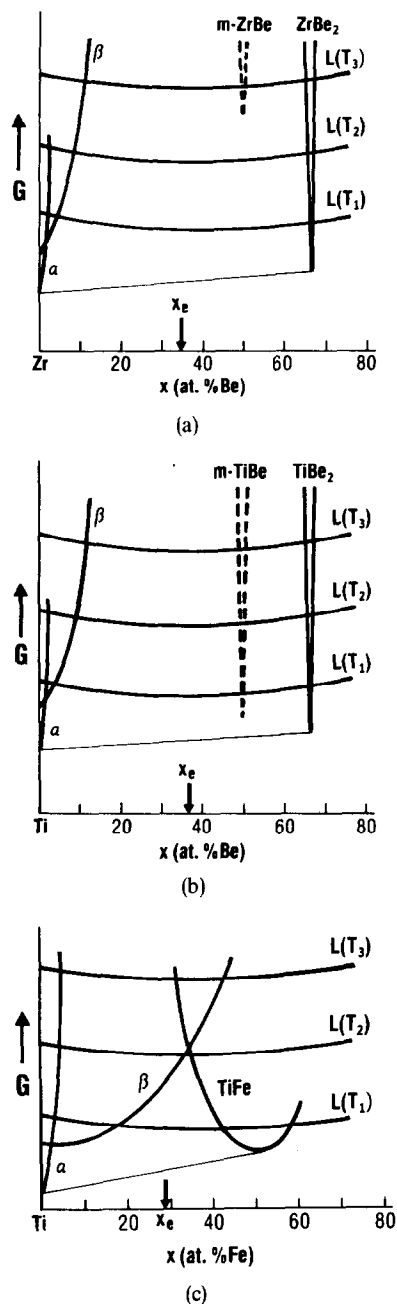


Fig. 11. Hypothetical free energy vs composition diagrams for binary systems including eutectic reactions and intermediate phases. (a) Zr-Be. (b) Ti-Be. (c) Ti-Fe (from Ray, Ref. [45]).

long-range diffusion, that is, if it cannot go directly to the glassy state.

Ramachandrarao *et al.* [41] noted that the predendritic (spherical) growth can subsequently develop into dendritic growth, when constitutional supercooling destabilizes the spherical growth front, which then allows solute to be rejected laterally [43]. This accounts for our observation of multiphase dendritic projections emanating from the β predendrites in $\text{Zr}_{90}\text{Be}_{10}$ [Fig. 2(d)]. Both electron and X-ray diffraction data indicate that the *minimum* lattice par-

ameter for retained β is found in this alloy, viz. $a_0 = 0.3550 \text{ nm}$, and that it remains unchanged at higher x (see Table 2). Thus, considering the above interpretation, it is reasonable to fix the maximum supersaturation at $\sim 10 \text{ at. \% Be}$. Accordingly, $\bar{V}_{\text{max}}^{\beta} = 22.403 \times 10^3 \text{ nm}^3$, and when plotted in Fig. 3, this value falls on an extension of the \bar{V}^{β} vs x_{Be} curve.

Ti-Be alloys exhibit comparable behavior. The maximum supersaturation in α' corresponds to the equilibrium solubility of Be in β (viz. $\sim 5 \text{ at. \%}$, cf. Figs. 5, 6 and Table 2). The maximum β supersaturation was estimated to be $\sim 15 \text{ at. \%}$ in the same manner described above for $\text{Zr}_{90}\text{Be}_{10}$. The corresponding lattice parameter observed in $\text{Ti}_{85}\text{Be}_{15}$ is $a_0 = 0.3211 \text{ nm}$ giving $\bar{V}_{\text{max}}^{\beta} = 16.556 \times 10^3 \text{ nm}^3$, which is also found to roughly follow the extension of supersaturation in α' as is shown in Fig. 6.

The extent of supersaturation will vary with alloy system and is primarily determined by the curvature of the G vs x function of the solid phase as it is related to the free energy curves for the liquid. A relatively extreme curvature [e.g. G_{S}^{II} in Fig. 10(b)] will tend to restrict the change in C_i with increasing x , as is shown by the path of curve T_0^{II} in Fig. 10(a); this seems to best represent the conditions for β in both Zr-Be and Ti-Be. On the other hand, a more shallow curvature, viz. G_{S}^{I} in Fig. 10(a), allows T_0^{I} to approach the eutectic composition x_e without too large an undercooling. The latter condition is typical of certain simple eutectic systems and results in the formation of a continuous series of solid solutions when splat-quenched, e.g. Cu-Ag [44]. In a similar manner, it is likely that a relatively shallow β free energy curve is at least partially responsible for the large extension of β solubility, as opposed to glass formation, in the Ti-Fe and Ti-Co systems [45, 46].

Extrapolation of the β and α' values of \bar{V} to pure Ti indicate that $\bar{V}_{\text{Ti}}^{\alpha} \approx \bar{V}_{\text{Ti}}^{\beta} (= 17.557 \times 10^3 \text{ nm}^3)$ at room temperature. This can be obtained by extrapolation of the β lattice parameters in Ti-Zr alloys [18] and was also confirmed by Giessen and co-workers [46, 47] in other Ti-based alloy systems. The values of \bar{V} in Zr-Be and Ti-Zr [18] also agree, giving $\bar{V}_{\text{Zr}}^{\alpha} \approx \bar{V}_{\text{Zr}}^{\beta} (= 23.271 \times 10^3 \text{ nm}^3)$. Ray [45] obtained a somewhat higher value, viz. $\sim 23.75 \times 10^3 \text{ nm}^3$ by extrapolation of supersaturated β lattice parameters from single-phase splat-quenched Zr-T alloys, where T is Mn, Fe, Co or Ni. On the other hand, the data from splat-cooled Zr-Rh alloys measured by Togano and Tachikawa [48] gives $\bar{V}_{\text{Zr}}^{\beta} \approx 22.75 \times 10^3 \text{ nm}^3$. Russell [49] reported still lower $\bar{V}_{\text{Zr}}^{\beta} (= 22.281 \times 10^3 \text{ nm}^3)$, where he assumed that the presence of 1.62 at. \% U has a negligible effect on a_0 . The latter $\bar{V}_{\text{Zr}}^{\beta}$ is felt to be too low and we are inclined toward the higher values. However, more precise measurements may be necessary to establish a reliable room-temperature value for the mean atomic volume of β -Zr.

4.1.2. Metastable ordered phases. From our observations, we can extend the representation of the thermo-

dynamic relationships between solid solutions and the liquid to include ordered phases. Schematic G vs x plots for the Zr-Be and Ti-Be systems are given in Figs. 11(a) and (b), respectively, where the temperature dependences of G_S and G_L are the same as those assumed for construction of the curves in Fig. 10(b). The persistent presence of the MOP m -TiBe in as-quenched microstructures, as well as its appearance as an initial reaction product during devitrification, indicate that this phase should have a free energy only slightly higher than those of stable Ti-Be phases [Fig. 11(b)], and this justifies its extension of metastability to low \dot{T} in Fig. 9. G for m -TiBe is also shown to be a very narrow function of x , since experiments do not reveal any significant degree of non-stoichiometry [33].

In contrast, m -ZrBe is almost invariably bypassed during liquid-quenching and was never observed during devitrification. Therefore, it is judged to have a substantially higher free energy relative to those of the stable Zr-Be phases as is depicted in Fig. 11(a), and accordingly, it is confined to the high \dot{T} range in Fig. 8. Kinetic factors could also have some bearing here. It is conceivable that the m -TiBe phase is also more easily nucleated from the liquid since it is one of the simplest of ordered crystalline configurations, viz. it has a cubic B2 (CsCl-type) structure [18]. m -ZrBe on the other hand, has a more complex orthorhombic B_f (CrB-type) structure [18], and so may require a relatively higher critical energy for nucleation under equivalent solidification conditions.

The identification of the MOP m -TiBe and the rationalization of its presence in the Ti-Be system in terms of crystal chemical and atomic size factors have been discussed in detail elsewhere [33]. Similar reasoning, using the compilations of Pearson [50], may also be invoked for m -ZrBe. However, this will be deferred to the discussion of the isomorphous m -HfBe phase in a subsequent report on the Hf-Be system [20] in which the MOP plays a more significant role in the critical phase relations.

Returning briefly to thermodynamic factors, we can compare G vs x for Ti-Be in Fig. 11(b) with the hypothetical free energy relationships in the Ti-Fe system as indicated by the results of Ray *et al.* [45, 46]. It was noted in Section 4.1.1 that β in the latter system shows a large extension of supersaturation suggesting that G_β should have a relatively shallow curvature as we show in Fig. 11(c). The same should also be true for G_{TiFe} , since TiFe(B2) is known to have an extended range of composition at equilibrium [51]. Thus, the relative shapes and locations G_{TiFe} and G_L shown in Fig. 11(c) provide a more complete explanation for the metastable extension of b.c.c. β from 22 to 35 at.%Fe and the continuous transition to the related cubic B2 structure of TiFe from 35–50 at.%Fe, all of which supercede glass formation during ultra-rapid quenching [45, 46, 56].

4.2 The glass state

4.2.1 Glass formation. According to Cohen and Turnbull [52], any liquid should form a glass if crystallization can be avoided. In metallic systems, this invariably requires unusually high \dot{T} ; consequently, the glass forming tendency (GFT) of an alloy is determined by rather stringent thermodynamic, kinetic, and structural factors [9]. It is well documented that the constitutional conditions resulting in eutectic formation (viz. decreasing T_l with x) tend to favor GFT, particularly if the eutectic is deep and the composition range is free of strongly competing metastable phases. Most of the glass formation models [9, 10, 27], whether primarily thermodynamic, kinetic, or electronic in origin, incorporate this alloying behavior and emphasize the stabilization of the liquid relative to a crystalline mixture. Chen's [27] thermodynamic arguments alternatively stress that GFT stems from a destabilization of the crystalline state. For the moment at least, each of these models seems to have difficulties in providing an adequate quantitative explanation for all the critical aspects of metallic glass formation.

Table 3. Glass forming characteristics of certain Zr and Ti based binary systems

System A-B	$x_B = 20 \text{ at. \%}$		$x_B = x_e \text{ (at. \%)}$		Glass Formation Range(a)		Ref.
	ΔT	$\Delta T/T_g^\circ$	ΔT	$\Delta T/T_g^\circ$	x_B	$x_B \text{ (at. \%)}$	
Zr-Be	100	0.057	322	0.206	34.5	30 – 50 (s) 30 – 45 (r)	(b)
Zr-Mn	90	0.063	145	0.103	32.5	45 – 50 (s)	45
Zr-Co	370	0.209	487	0.280	22	27 – 60 (s) 27 – 40 (r)	45, 55 56
Zr-Fe	400	0.236	480	0.282	24	30 – 35 (s) 25 – 35 (r)	45 56
Zr-Ni	385	0.218	467	0.275	24	24 – 70 (s) 24 – 42 (r)	45, 55 56
Zr-Pd	250	0.141	397	0.234	24.5	33 – 45 (s) 25 – 35 (r)	45, 55 56
Zr-Rh	270	0.153	342	0.204	25	17 – 28 (s)	48
Ti-Be	0	—	47	0.035	37.5	37 – 41 (s)	(b)
Ti-Ni	210	0.128	325	0.211	29	30 – 45 (s) 30 – 40 (r)	57 56
Ti-Co	285	0.174	375	0.225	24.5	none	45, 56
Ti-Fe	105	0.064	132	0.089	24	none	46, 56
Ti-Si	—	—	137	0.079	13.8	20 (s)	57

(a) (s) is for splat-quenched foils; (r) is for ribbon fabrication.

(b) Present work.

Turnbull [53] suggested that GFT should be enhanced if a eutectic is 'abnormally deep', viz. if it falls below predictions based on ideal solution theory. Marcus and Turnbull [54] compared the GFT of various systems based on this concept with reasonable success. Whereas these authors were principally concerned with metal/metalloid glass-formers, we will examine relative GFT for metal (A)/metal (B) systems in which the solvents A are Zr or Ti. Following Marcus and Turnbull [54], we have computed the reduced liquidus depression

$$T_{rl}^0(x) = \Delta T/T_l^0(x) = [T_l^0(x) - T_l(x)]/T_l^0(x)$$

where $T_l^0(x)$ is the liquidus temperature based on ideal solution theory and $T_l(x)$ is the observed liquidus temperature, both at a given solute B concentration x . We have chosen to make comparisons at $x = 20$ at.%B since the eutectic compositions for most of these systems are $20 < x_e < 26$, with only a few between 26–38 at.%B. Computations were also made at $x = x_e$. The results are listed in Table 3, along with the experimentally observed glass formation ranges. In general, all these glass formers require relatively high cooling rates, at least 10^6 – 10^7 K s⁻¹. Accordingly, we find that for the majority of Zr-based glasses, $T_{rl}^0 > 0.14$ (at $x = 20$) or > 0.2 (at $x = x_e$); and for the most difficult glasses to form, which are those in the Zr-Mn system [45], $T_{rl}^0 = 0.063$ (at $x = 20$) or 0.103 (at $x = x_e$). An apparent exception is Zr-Be which experimentally fits with the former group, but T_{rl}^0 at 20 at.% is only 0.057. However, at x_e , T_{rl}^0 is 0.206 and thus falls into the appropriate range; hence, the former value is likely due to a poor experimental approximation of the liquidus [16].

The comparisons for the Ti-based alloys seem to be a less reliable indicator of GFT. Both Ti-Ni and Ti-Be alloys are particularly difficult glass formers, with Ti-Ni appearing to require only slightly lower critical cooling rates [45, 56, 57]. Yet, $T_{rl}^0(x_e)$ is 0.211 for Ti-Ni compared to an expected low value of 0.035 for Ti-Be. Furthermore, Ti-Co and Ti-Fe do not form glasses at all [45, 46, 56], and their values at x_e are 0.225 and 0.089, respectively. At this point it is difficult to establish the source(s) of these apparent inconsistencies. As noted above, at least part of the problem may stem from experimental inaccuracies regarding the course of the liquidus curves. However, it is also possible that the approximations of the ideal solution model are too limited and more detailed computations utilizing T_0 vs x relationships, as discussed in Sections 4.1.1 and 4.1.2, are required. However, taking the values in Table 3 at face value, this approximate test of GFT indicates that Zr-Be glasses should indeed be more easily formed than those of Ti-Be.

Another factor that apparently affects GFT is the nominal size ratio of the constituent elements. Readily formed metallic glasses usually have atomic radii ratios r_A/r_B in the range 1.15–1.25 [9]. Table 4 shows that all the systems listed in Table 3 meet this cri-

terion and furthermore, Zr-Be and Ti-Be alloys have even more favorable size differences. Hence, size factor is not an effective GFT indicator here.

This now brings us to the analysis of relative glass formability in terms of transformation kinetics. Davies and co-workers [32], utilizing formulations for the computation of isothermal TTT (time-temperature-transformation) diagrams developed by Uhlmann [58, 59], have determined values of \dot{T}_c , the critical cooling rate to just avoid crystallization, for a wide variety of metals and alloys. A correlation of \dot{T}_c can be made with the reduced glass temperature T_{rg} ($= T_g/T_m$, where T_m is the melting temperature) and this is primarily realized through the approximations used to determine the temperature variation of viscosity, η . The Davies work shows an approximate monotonic increase of $\log \dot{T}_c$ with decreasing T_{rg} , where the corresponding ranges are $10^2 < \dot{T}_c < 10^{10}$ K s⁻¹ and $0.65 > T_{rg} > 0.2$ (see Fig. 6 in Ref. [32]). As a specific example, Davies [32] calculated $\dot{T}_c = 7 \times 10^3$ K s⁻¹ for Pd₈₂Si₁₈ and $\dot{T}_c = 2 \times 10^2$ K s⁻¹ for Pd_{77.5}Cu₆Si_{16.5} in good agreement with experiment. The higher \dot{T}_c of the binary was principally associated with the 5% lower value of its T_{rg} (T_{rg} is 0.603 and 0.633 for the Pd-Si and Pd-Cu-Si glasses, respectively).

Application of these formulations in a like manner to the Zr-Be and Ti-Be eutectic composition glasses give nearly identical values of \dot{T}_c (viz. 2.5×10^7 and 1.2×10^7 K s⁻¹, respectively), whereas T_{rg} for Zr₆₅Be₃₅ is ~2.5% greater than that for Ti₆₃Be₃₇ (viz. 0.516 and 0.503, respectively). These \dot{T}_c s, while reasonably close to the experimentally indicated high cooling rates, do not reflect the estimated one (perhaps two) orders of magnitude higher rate required for glass formation in the Ti-Be alloy (cf. Figs. 8 and 9). Furthermore, there is no apparent correlation with the associated values of T_{rg} as predicted by Davies [32].

The above opens the question of whether the Davies-Uhlmann (DU) kinetic formulations properly

Table 4. Ratios of atomic radii for certain Zr and Ti based binary systems

System A-B	r_A/r_B (b)
Zr-Be	1.42
Zr-Mn	1.27
Zr-Co	1.28
Zr-Fe	1.26
Zr-Ni	1.29
Zr-Pd	1.16
Zr-Rh	1.19
Ti-Be	1.30
Ti-Ni	1.17
Ti-Fe	1.15
Ti-Co	1.17
Ti-Si(a)	1.11

(a) In Ti₅Si₃, r_A/r_B observed to be 1.20.

(b) Values obtained from compilations appearing in Ref. [50].

represent all factors involved in glass formation. Davies [32] did consider the numerical effect of various sources of uncertainty. With all terms considered (aside from the well-known problems related to estimating the temperature dependence of viscosity between T_m and T_g) the only parameter that could be a likely source of the difficulty being experienced here is ΔG^* , the free energy barrier to homogeneous nucleation of a crystalline phase. The values of \dot{T}_c quoted above were all calculated assuming ΔG^* to be the same for each system [32, 58]. However, this is not implied in previous analyses [60] and has indeed been questioned in recent reports by Jones [38], Lewis and Davies [61], Onorato and Uhlmann [62], Spaepen and Turnbull [10], Boswell and Chadwick [63] and Klein *et al.* [64]. In the following, we rederive the nucleation frequency term of the DU treatment specifically so as to eliminate any ambiguities. This then facilitates reasonable adjustments of ΔG^* and allows us to examine the effect(s) on \dot{T}_c . We will also develop an alternative form for the ΔG^* relationship which includes a temperature dependence of the liquid-solid interfacial tension as was recently proposed by Spaepen and Meyer [65, 66].

The transformation formalisms used in the DU treatment have their origins in the early works of Johnson and Mehl and of Avrami [67]. X , the fraction of transformed volume of liquid to single phase crystal of the same composition in time t is given by

$$X \approx \frac{\pi}{3} \cdot I_V u_c^3 t^4, \quad (1)$$

where I_V is the crystal nucleation frequency per unit volume and u_c is the rate of crystal growth; both terms are time independent [67].

Thermally activated, steady-state, homogeneous nucleation frequency I_V^h is given by

$$I_V^h = \frac{D_n \bar{N}_V}{a_o^2} \cdot \exp\left(-\frac{\Delta G^*}{kT}\right), \quad (2)$$

where D_n is an atomic diffusion coefficient characteristic for atomic motion necessary for crystallization at temperature T , \bar{N}_V is the average concentration of atoms per unit volume, a_o is the mean atomic diameter, ΔG^* was defined above and k is Boltzman's constant.

ΔG^* is related to the liquid-solid interfacial tension per unit area σ and to the volume free energy ΔG_V as follows:

$$\Delta G^* = \frac{16\pi}{3} \cdot \frac{\sigma^3}{(\Delta G_V)^2}, \quad (3)$$

where the thermodynamic driving force is given by

$$\Delta G_V = T_r \Delta T_r \Delta H_f^l,$$

which includes the effect of a difference in heat capacity between liquid and crystal [68]. T_r is the reduced melting temperature T/T_m , ΔT_r is the reduced undercooling $(T_m - T)/T_m$ and ΔH_f^l is the enthalpy of

fusion per unit volume. From Turnbull [60, 69], the molar interfacial tension is

$$\sigma_M = K' \sigma V^{2/3} N_o^{1/3},$$

where N_o is Avogadro's number, V is the molar volume and K' is a structural factor of order unity. σ_M can also be expressed in the form

$$\sigma_M = \alpha V \Delta H_f^l,$$

where α is the reduced interfacial tension defined as the number of monolayers per unit area of crystal which would be melted by an enthalpy equivalent to σ_M [10]. Further, the enthalpy of fusion evaluated at $T = T_m$ is given by [60, 69].

$$\Delta H_f^l = \frac{N_o k \beta T_m}{V}. \quad (4)$$

Substituting in equation (3) we now have

$$\frac{\Delta G^*}{kT} = \frac{16\pi}{3(K')^3} \cdot \alpha^3 \beta \cdot \frac{1}{\Delta T_r^2 T_r^3}. \quad (5)$$

Now, Spaepen [65] and Spaepen and Meyer [66] have suggested that the melt tension σ_M is primarily entropic in origin, based on a dense-random-packing model of the liquid-solid interface; accordingly σ_M becomes a temperature dependent term, thus

$$\alpha = \alpha_m T_r,$$

where α_m is the value at T_m . This provides an alternative version of equation (5), namely

$$\frac{\Delta G^*}{kT} = \frac{16\pi}{3(K')^3} \cdot \alpha_m^3 \beta \cdot \frac{1}{\Delta T_r^2}. \quad (6)$$

Following previous derivations [32, 58] crystal growth rate is

$$u_c = \frac{f D_g}{a_o} \left[1 - \exp\left(-\frac{\Delta T_r \Delta H_f^l}{RT}\right) \right], \quad (7)$$

where ΔH_f^l is the molar enthalpy of fusion, R is the gas constant, f is the fraction of sites available at the growth interface and D_g is a diffusion coefficient for atomic motion required for crystal growth.

After Davies [32], it is assumed that $D_n = D_g = D$, the bulk liquid diffusion coefficient, and is related to the bulk liquid viscosity η by the Stokes-Einstein equation

$$D = \frac{kT}{3\pi a_o \eta}.$$

We can now substitute for D in the expressions for I_V^h and u_c , incorporate equations (2) and (7) into equation (1) and then, by rearranging terms in the manner of Davies [32], we obtain

$$t \approx \frac{9.3\eta}{kT} \left\{ \frac{\frac{a_o^2 X}{f^3 N_V} \left[\exp\left(\frac{\Delta G^*}{kT}\right) \right]}{\left[1 - \exp\left(-\frac{\Delta H_f^l \Delta T_r}{RT}\right) \right]^3} \right\}^{1/4}, \quad (8)$$

Table 5. Property values assumed for Zr-Be and Ti-Be eutectic alloys

	Zr ₆₅ Be ₃₅	Refs.	Ti ₆₃ Be ₃₇	Refs.
T _g (K at $\eta = 10^{13}$ P)	623	(a)	673	(a)
T _m (K at x_e)	1238	28	1303	16
a ₀ (nm)	0.287	50	0.269	50
\bar{N}_V (atoms m ⁻³)	5.3×10^{28}	(a)	7.37×10^{28}	(a)
f	1	58,59,71	1	58,59,71
X	10^{-6}	32,58	10^{-6}	32,58
ΔH_M^f (J · mol ⁻¹)	15.4×10^3	70	15.3×10^3	70
η (P)	$\eta = 0.0334 \exp(f_T^{-1})$ $f_T = 3.895 \exp\left(-\frac{5935}{RT}\right)$	72, (a)	$\eta = 0.0334 \exp(f_T^{-1})$ $f_T = 4.829 \exp\left(-\frac{6795}{RT}\right)$	72, (a)

(a) This work.

where the appropriate expressions for ΔG^* will be chosen later.

The TTT diagrams are computed for the formation of a barely detectable volume fraction of crystal, viz. $X \approx 10^{-6}$. Other property values and relationships to be substituted in equation (8) are listed in Table 5. Values of a_0 for the pure components were obtained from Pearson [50] and adjusted for alloy composition. \bar{N}_V values were calculated from our density measurements. Values of ΔH_M^f are not available from experiment, but may be estimated from the thermodynamic computations for these systems made by Kaufman and Nesor [70]. The crystalline interface site fraction $f = 1$ denoting a rough surface (viz. one of high ledge population) characteristic of alloys having relatively low entropies of fusion, i.e.

$$\Delta S_M^f = \frac{\Delta H_M^f}{T_m} < 2R$$

[58, 59, 71].

Following Ramachandrarao *et al.* [72], the temperature dependence of viscosity may be represented by a Doolittle-type expression involving the relative free volume [73]. This approach has been shown to provide somewhat improved approximations of η over the full range of T_m to T_g for Au₇₇Ge_{13.6}Si_{9.4}, Pd_{77.5}Cu₆Si_{16.5} and Pd₈₂Si₁₈ than those used by Davies *et al.* [32]. Expressions derived from T_m , T_g and $\eta = 10^{13}$ P at T_g for Zr₆₅Be₃₅ and Ti₆₃Be₃₇ are given in Table 5.

In the original DU treatment [32, 58], it was assumed that $\Delta G^* = 50$ kT at $\Delta T_r = 0.2$ [74]. Now it is our view that the difference in glass forming behavior observed here stems from a lower barrier to crystallite nucleation in the Ti-Be alloy; accordingly, we have varied ΔG^* from 35 kT to 50 kT for Ti₆₃Be₃₇ and from 50 kT to 65 kT for Zr₆₅Be₃₅, for $\Delta T_r = 0.2$. The two TTT curves plotted in Fig. 12(a) are examples which illustrate the effect of a moderate dif-

ference in ΔG^* , viz. 40 kT and 55 kT at $\Delta T_r = 0.2$, where equation (5) was used for evaluating $\Delta G^*/kT$. The dashed curves in the figure correspond to the modification for the effect of continuous cooling using the Grange-Kiefer method [62, 63, 75], and these are the curves used for the determination of \hat{T}_c as follows:

$$\hat{T}_c = \frac{T_m - T_N}{t_N},$$

where T_N and t_N locate the nose of the CCT (Continuous Cooling Transformation) curves. The values for the curves in Fig. 12(a) are 3.4×10^7 and 4.6×10^6 K s⁻¹ for Ti-Be (with $\Delta G^* = 40$ kT) and Zr-Be (with $\Delta G^* = 55$ kT), respectively, and the full listing of \hat{T}_c 's is given in Table 6. Figure 12(b) contains curves for the same values of ΔG^* as in Fig. 12(a) using the kinetics equation that incorporates a temperature dependence of σ_m [10, 61] through substitution of equation (6) in place of equation (5). Here we find that 40 kT gives 3.0×10^8 K s⁻¹ and 55 kT gives 7.6×10^7 K s⁻¹, a factor of 4 difference in \hat{T}_c ; the remaining values are listed in Table 6. It is clear that the change in the form of equation (8) has two effects: first, it seems to overestimate the values of \hat{T}_c by about one order of magnitude [61] when compared to our evaluation of the experimental cooling conditions (cf. Figs. 8 and 9). Second, it requires a larger spread between ΔG^* (viz. 35 kT and 60 kT, see Table 6) to obtain a factor of 10 difference between the two alloy systems. Hence, the original DU treatment appears to give better agreement with experiment for comparable variations of ΔG^* . It is worth noting here that recent experiments on the large undercooling of droplets of certain low-melting metals and alloys by Perepezko *et al.* [76] do not support the concept by Spaepen and Meyer [65, 66] that σ_m is a temperature dependent term.

The extent to which ΔG^* can be varied has not been established [38]. Limited experimental observa-

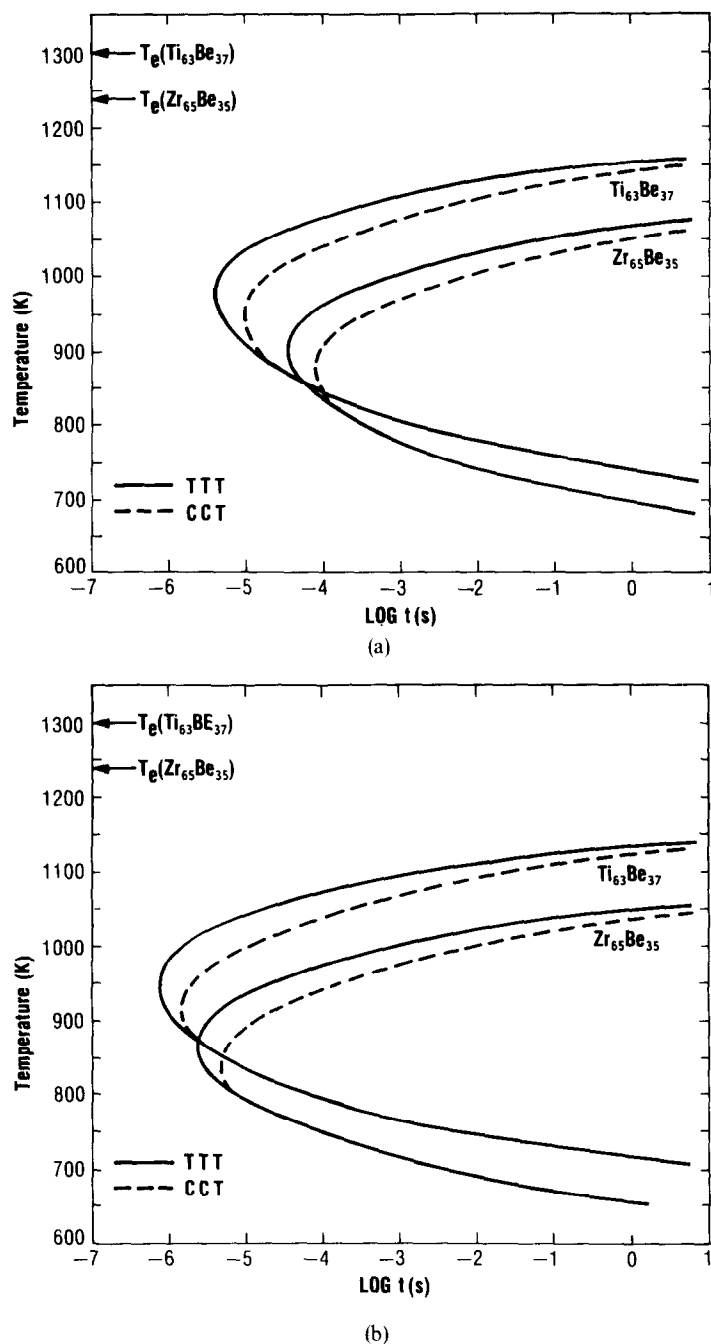


Fig. 12. Computed liquid-to-solid transformation diagrams for eutectic compositions of Zr-Be and Ti-Be alloys using equation (8) in the text and showing the effect of varying the value of the critical free energy barrier to crystal nucleation ΔG^* . (a) Original Davies-Uhlmann (DU) treatment using equation (5) for ΔG^* (i.e. solid-liquid surface energy assumed *not* to be temperature dependent). ΔG^* at $\Delta T_r = 0.2$ is 40 kT for $\text{Ti}_{63}\text{Be}_{37}$ and is 55 kT for $\text{Zr}_{65}\text{Be}_{35}$. (b) Modified DU treatment using equation (6) for ΔG^* (i.e. solid-liquid surface energy assumed to be temperature dependent). Once again, ΔG^* at $\Delta T_r = 0.2$ is 40 kT for $\text{Ti}_{63}\text{Be}_{37}$ and is 55 kT for $\text{Zr}_{65}\text{Be}_{35}$. The critical cooling rate to avoid nucleation \dot{T}_c was obtained from the position of the nose of the CCT curves (see text).

tions suggest that the variation may only be about $\pm 5\%$ [74]. However, Lewis and Davies [61] have considered that using $\Delta G^* = 50 \text{ kT} \pm 10 \text{ kT}$ may be appropriate for their generalized model. Onarato and Uhlmann [62] increased ΔG^* to 65 kT in order to

explain certain oxide glass forming behavior. On the other hand, Klein *et al.* [64] reduced the value to 45 kT for another oxide glass; and Boswell and Chadwick [63] required a decrease to 42 kT to obtain agreement with observed grain size variations in

Table 6. Effect of homogeneous nucleation barrier on calculated critical cooling rates for glass formation

ΔG^* (at $\Delta T_f = 0.2$)	Critical Cooling Rate, \dot{T}_c ($K \cdot s^{-1}$) (a)			
	Original DU Treatment(b)		Modified DU Treatment(c)	
	Zr ₆₅ Be ₃₅	Ti ₆₃ Be ₃₇	Zr ₆₅ Be ₃₅	Ti ₆₃ Be ₃₇
35kT		1.4×10^8		4.7×10^8
40kT		3.4×10^7		3.0×10^8
45kT		1.5×10^7		1.3×10^8
50kT	1.0×10^7	6.3×10^6	1.3×10^8	7.7×10^7
55kT	4.6×10^6		7.6×10^7	
60kT	1.7×10^6		4.8×10^7	
65kT	7.3×10^5		2.5×10^7	

(a) Computed for CCT curves, see Figs. 12(a) and 12(b).

(b) Equation (5) used in equation (8), see text.

(c) Equation (6) used in equation (8), see text.

splat-quenched crystalline Al and Al-rich alloys. In all of the cases cited, the original DU formulation was used.

We can look further and try to gain some insight as to the possible source(s) of changes in ΔG^* . Of the terms in equations (5) and (6), only α (or α_m) and β can be considered [10, 38]. β is approx. 1.4 for both these systems [see equation (4) and Table 5] and these values may change somewhat with exact determinations of ΔH_M ; however, this is unlikely to have a profound effect on the kinetics, since any change in ΔH_M is likely to be relatively small and β is only raised to the first power. In contrast, α_m is a cubed term, and while it is believed to vary rather little from system to system [10, 65, 66], a small change in α_m could have a significant effect on ΔG^* [77]. For example, Spaepen and Meyer [66] suggested that an upper limit in metallic alloys may be $\alpha_m \approx 0.86$. In the extreme, if this value corresponds to $\Delta G^* = 60$ kT at $\Delta T_f = 0.2$, then for a value of 35 kT, $\alpha_m \approx 0.72$, a change of only about 16%. The smaller differences in ΔG^* also considered earlier, viz. 55 kT and 40 kT shown in Fig. 12, would result in α_m of 0.86 and 0.77, respectively, or an 11% difference. Such variations in α_m may prove to be within reason [10, 64, 78].

In summation then, we have shown that both the original and the modified versions of the DU kinetic treatment successfully predict the high magnitude of cooling rates required to form glasses in Zr-Be and Ti-Be eutectic alloys. However, it is only when the nucleation barrier to crystallization in Ti-Be is lowered relative to that for Zr-Be, that an approximate match can be made with the observed difference in GFT between these alloys. The adequacy of the above analysis must await a further assessment of parameters and their specific values used in nucleation and growth theories as applied to the ultra-rapid solidification of metallic liquids.

4.2.2 Devitrification. The sequence of devitrification processes may follow varied paths which, like metastable phase formation on cooling, are critically

dependent on interrelated thermodynamic, kinetic and structural factors [38]. Upon reheating, an alloy glass may transform to single or multiple metastable crystalline states prior to reaching its equilibrium microstructure or, as in the case of Zr-Be glasses, the transformation can proceed directly to its final state. In the latter case, there are indications from the relative disposition of the exothermic DSC peaks [see Figs. 1(e) and 4] and XRD phase identification at each stage, that the development of structure during devitrification of Zr-Be glasses involves: (i) the formation of primary equilibrium α initially (particularly in hypoeutectic compositions); (ii) subsequent co-precipitation of $\alpha + \text{ZrBe}_2$ (perhaps similar in form to the multiphase nodules observed by TEM in $\text{Pd}_{78.1}\text{Cu}_{5.5}\text{Si}_{16.4}$ [79] and $\text{Fe}_{80}\text{B}_{20}$ [80, 81]); and (iii) culminating in a coarsening and/or recrystallization stage to produce final equilibrium assemblies. The foregoing analyses are speculative, and will be replaced by a more definitive description of the evolution of microstructures when TEM examinations have been completed [82].

The devitrification sequence for Ti-Be glasses is more complicated. Primary equilibrium α is always the initial reaction product, followed by the independent formation of the metastable ordered phase (MOP) $m\text{-TiBe}$. The reversion temperature of the MOP and subsequent formation of equilibrium TiBe_2 could not be firmly established. However, anomalies in DTA thermograms, discussed earlier, suggest that the processes may occur in the vicinity of the $\alpha \rightarrow \beta$ transformation at $\sim 825^\circ\text{C}$. Furthermore, the reversion may be complicated by interaction with oxygen and/or nitrogen, where the latter is either present in the alloys as an impurity or enters the DTA cell during operation. The η phase is formed easily at elevated temperatures as described earlier and this reaction may be enhanced through a diffusion controlled transformation of the MOP $m\text{-TiBe}$; however, this has not been established unambiguously and will be discussed further elsewhere [35].

The Ti-Be devitrification sequence can be viewed in terms of the relative positions of free energy curves and consequent relative displacements of CCT curves for down-quenching and CHT (Continuous Heating Transformation) curves, etc. [77, 81, 83]. During rapid quenching, the liquid is well beyond the normal eutectic crystallization of $\beta + \text{TiBe}_2$ and, as described earlier, must avoid the nose of the curve related to the formation of supersaturated β and/or $m\text{-TiBe}$ in order to form a glass. On reheating the glass, both kinetic and thermodynamic factors favor the formation of the low-temperature stable α solid solution [77, 81, 84]. At slightly higher temperatures, however, $m\text{-TiBe}$ preempts the formation of equilibrium TiBe_2 . This may be due to a combination of one or more factors including: (i) the apparent small difference in free energy of $m\text{-TiBe}$ relative to other Ti-Be phases, (ii) that $m\text{-TiBe}$ has a simpler ordered crystal structure than TiBe_2 [18] and/or (iii) that its formation requires a smaller variation in composition, viz. an increase to only 50 at.%Be compared to 67 at.%Be to form TiBe_2 .

4.3 Thermal and physical properties of the glasses

The thermal stability of metallic glasses, as characterized by the glass transition temperature, T_g , and their mechanical behavior at ambient temperatures are widely measured properties. They quite often exhibit remarkably similar compositional dependences and consequently, this had led to consideration of their possible interdependence [85]. Most of the data have been obtained from multicomponent alloys for which the effects of the individual elements could not always be separated.

The present work on Zr-Be provides information on a binary system with a sufficiently large glass formation range to allow unambiguous composition trends to be observed. Figure 1(d) shows that hardness (H_v) increases as Be increases from hypo- to hypereutectic compositions over a span of 20 at.%. In Fig. 1(e) we can see that T_g follows a rather similar path. Identical behavior was also recently observed in binary Hf-Be glasses between 30 and 60 at.%Be, where the eutectic x_e is at ~ 42 at.% [20]. Of the metal/metalloid glasses, data have been gathered for Fe-B over the range 13–26 at.%B ($x_e = 18$ at.%) [86] and both H_v and Young's modulus increase with increasing B content. T_g 's are not accessible here, but the start of crystallization (T_c), often a reasonably effective substitute, exhibits a corresponding increase from 13–17 at.%B; the trend breaks down at $17 < x < 26$ where the crystallization process appears to be accelerated. The glass forming range in binary Pd-Si was recently expanded to 15–25 at.%Si [87] ($x_e = 18$ at.%); only T_g was measured and here too, an increase with the increase in minority element was observed.

The origin and magnitude of T_g have been variously discussed [9, 24, 53, 59] and the consensus has focused on a direct proportionality with atomic cohesive energy. For example, this has been manifested through its relation to the height of the potential barrier for cooperative atomic transport [32], a scaling with the temperature of boiling [59] or with the enthalpy for vaporization [32], etc. The discussions of mechanisms for mechanical deformation have been more varied and complex [88–92], however, a primary association is most often made with the resistance to cooperative atomic rearrangement and hence, to the bonding energy between atoms in a given alloy. The principal arguments to explain the composition dependences have been put forth by Chen and co-workers [23, 93, 94]. Chen sees that metallic glasses maintain a characteristic (though unspecified) short-range order, and recent EXAFS results confirm this concept [95]. Gilman [96] has suggested certain possible clusters in eutectic, or near-eutectic liquid compositions that could be inherited by the corresponding glasses.

The compositional ordering, which arises from strong interactions between unlike A and B atoms [23], progressively increases as the minority B atom population increases. This, in turn, enhances a primary effect of the interactions, namely it raises T_g . Chen [23] has also argued that there is an accompanying increase in structural ordering, which may be analogous to the improved packing and associated increase in energy per bond with increasing B atom concentration revealed by recent computer simulations of glass structures by Boudreaux [97]. This would be expected to hinder internal displacements and hence result in increases of both hardness and elastic moduli as a function of composition. Obviously, these effects cannot continue indefinitely, but it is not unambiguously clear from the existing models how or when they saturate. There may be a link with the long-range ordering and associated bonding of the highest melting crystalline phase and the corresponding liquid of same composition in a given system [98], but this area has not been explored as yet.

5. SUMMARY AND CONCLUSIONS

Alloys Zr-Be and Ti-Be, up to ~ 70 at.%Be were quenched from the liquid at extremely high rates (viz. $\dot{T} > 10^6^\circ\text{C s}^{-1}$) and were found to form the glassy state over a range of compositions that bracket their respective eutectics. In addition, they exhibit Be supersaturation of their terminal solid solutions and also form metastable ordered phases. The salient features of the above for these two systems are the following:

	Zr-Be	Ti-Be
(1) Maximum supersaturation of β solid solution		
(a) transformed β (i.e. α')	5 at.%Be	5 at.%Be
(b) retained β	10 at.%Be	15 at.%Be

(2) Glass formation range	30–50 at.%Be ($x_e = 34.8$ at.%Be)	37–41 at.%Be ($x_e = 37.5$ at.%Be)
(3) Metastable ordered phases	<i>m</i> -ZrBe B_f (CrB-type) $a_o \approx 0.336$ nm $b_o \approx 1.028$ nm $c_o \approx 0.369$ nm	<i>m</i> -TiBe B2 (CsCl-type) $a_o = 0.2940$ nm
(4) Estimated critical cooling rate for glass formation (\dot{T}_c)	10^6 – 10^7 °C s ⁻¹	10^7 – 10^8 °C s ⁻¹

The observed values of \dot{T}_c , while semi-quantitative, are unambiguous since Ti-Be glass formation requires the higher cooling rates only available by means of arc-melting/hammer-and-anvil splat-quenching. On the other hand, the Zr-Be glasses are easily produced by the less rapid ribbon fabrication techniques. Computations of \dot{T}_c for these systems using the Davies-Uhlmann kinetic formulations give appropriately high values, but do not predict the 1–2 orders of magnitude higher \dot{T}_c required for glass formation in binary Ti-Be alloys. However, these calculations were found to be effective if ΔG^* , the free energy barrier to homogeneous nucleation of a crystalline phase, is taken to be lower in Ti-Be than in Zr-Be alloys. This variation could be realized through the assumption that the solid-liquid surface tensions in the two systems also differ in this manner. The required adjustments in these parameters appeared to be well within limits suggested by others. However, it is clear from these analyses that the parameters and their specific values used in nucleation and growth theories as applied to ultra-rapid solidification in metallic systems should be reassessed.

In Zr-Be, both the room-temperature hardnesses of the glasses and the glass transition temperatures T_g increase with increasing Be solute. These variations with composition have been discussed in light of recent ideas pertaining to short-range order in the liquid and glassy states.

NOTE: At the time of publication, the authors became aware of a new examination of crystal nucleation kinetics by Thompson and Spaepen [to be published in *Acta metall.* (1979)]. They have shown that expression for ΔG_v due to Hoffman [68] used here, and by Davies [32] and Uhlmann [58, 59], may not be appropriate for supercooled metals and alloys. A more suitable expression was derived and this will be incorporated in new calculations of \dot{T}_c for these glass-forming systems and for the Hf-Be glassy alloys [20].

Acknowledgements—The authors are deeply indebted to Mr. C. F. Cline for initiating this project and giving his supportive encouragement, to Ms. E. Musso and Mr. R. Costa for their invaluable technical assistance and to Ms. J. Napolitano for preparation of the manuscript. We also wish to thank our colleagues Drs. D. S. Boudreaux, C. P. Chou, L. A. Davis and R. Hasegawa for their helpful dis-

cussions and comments. Finally, special thanks are due to Dr. D. S. Boudreaux for his programming assistance, Prof. B. C. Giessen for his collaborative, as well as tutorial efforts with respect to the crystallography and crystal chemistry of stable and metastable phases, and Prof. F. Spaepen for discussions of transformation kinetics and a critical review of the original manuscript.

REFERENCES

1. J. J. Gilman, *Physics Today* **28**, 46 (May 1975).
2. J. J. Gilman, *Crystal Growth and Materials* (edited by E. Kaldis and H. J. Scheel), p. 728. North Holland, Amsterdam (1977).
3. *Rapidly Quenched Metals*, Section I (edited by N. J. Grant and B. C. Giessen). MIT Press, Cambridge, MA (1976).
4. *Rapidly Quenched Metals*, Section II (edited by N. J. Grant and B. C. Giessen). *Mat. Sci. Engng* **23**, 81–324 (1976).
5. *Metallic Glasses* (edited by J. J. Gilman and H. J. Leamy). ASM, Metals Park, OH (1978).
6. L. A. Davis, Ref. [3], p. 369; Ref. [5], p. 190.
7. R. Ray and S. Kavesh, U.S. Patent No. 4,036,638 (1977). METGLAS® is a registered trademark of Allied Chemical Corp., Morristown, NJ.
8. L. A. Davis, R. Ray, C.-P. Chou and R. C. O'Handley, *Scripta metall.* **10**, 541 (1976).
9. D. E. Polk and B. C. Giessen, Ref. [5], p. 1.
10. F. Spaepen and D. Turnbull, Ref. [3], p. 205.
11. L. E. Tanner and R. Ray, *Scripta metall.* **11**, 783 (1977).
12. L. E. Tanner and R. Ray, to be published; see also U.S. Patents Nos. 3,989,517 (1976) and 4,050,931 (1977).
13. M. Ohring and A. Haldipur, *Rev. Sci. Instrum.* **42**, 530 (1971).
14. S. Kavesh, Ref. [5], p. 36.
15. R. A. Spurling, *Metall. Trans.* **6A**, 1660 (1975).
16. R. P. Elliot, *Constitution of Binary Alloys*, First Supplement, p. 175. McGraw Hill, New York (1965).
17. J. C. Williams, *Titanium Science and Technology* (edited by R. I. Jaffe and H. M. Burte), Vol. 3, p. 1433. Plenum Press, New York (1973).
18. W. B. Pearson, *A Handbook of Lattice Spacings and Structures of Metals and Alloys*, Vol. 1. Pergamon Press, New York (1958).
19. B. C. Giessen, Ref. [3], p. 119.
20. L. E. Tanner, to be published; see also U.S. Patent No. 4,118,222 (1978).
21. T. B. Massalski, *Physical Metallurgy*, 2nd Edition, (edited by R. W. Cahn), p. 202. North Holland/American Elsevier, New York (1970).
22. G. S. Cargill III, *J. appl. Phys.* **41**, 2248 (1970).
23. H. S. Chen and B. K. Park, *Acta metall.* **21**, 395 (1973).
24. D. Turnbull, *Trans. Met. Soc. AIME* **221**, 422 (1961).

25. G. S. Cargill III, *Solid State Physics* (edited by H. Ehrenreich, F. Seitz and D. Turnbull), Vol. 30, p. 227. Academic Press, New York (1975).
26. H. S. Chen and E. Coleman, *Appl. Phys. Lett.* **28**, 2560 (1976).
27. H. S. Chen and K. A. Jackson, Ref. [5], p. 74.
28. Ref. [16], p. 172.
29. D. B. Hunter, *Trans. Met. Soc. AIME* **236**, 900 (1966).
30. B. C. Giessen and R. H. Willens, *Phase Diagrams, Materials Science and Technology* (edited by A. M. Alper), Vol. 2, p. 103. Academic Press, New York (1970).
31. B. C. Giessen and C. N. J. Wagner, *Liquid Metals, Chemistry and Physics* (edited by S. Z. Beer), p. 633. Marcel Dekker, New York (1972).
32. H. A. Davies, *Phys. Chem. Glasses* **17**, 159 (1976).
33. L. E. Tanner and B. C. Giessen, *Metall. Trans.* **9A**, 67 (1978).
34. H. H. Stadelmaier, *Developments in Structural Chemistry of Alloy Phases* (edited by B. C. Giessen), p. 141. Plenum Press, New York (1969).
35. B. C. Giessen, J. Barrick and L. E. Tanner, *Mat. Sci. Engng.* **38**, 211 (1979).
36. T. R. Anantharaman, H.-L. Luo and W. Klement, Jr., *Trans. Met. Soc. AIME* **223**, 2014 (1965).
37. R. Ruhl, *Mat. Sci. Engng* **1**, 313 (1967).
38. H. Jones, *Rep. Prog. Phys.* **36**, 1425 (1973).
39. R. Wang, Ref. [3], p. 135.
40. H. Biloni and B. Chalmers, *Trans. Met. Soc. AIME* **233**, 273 (1965).
41. P. Ramachandrarao, M. G. Scott and G. A. Chadwick, *Phil. Mag.* **25**, 961 (1972).
42. L. S. Darken and R. W. Gurry, *Physical Chemistry of Metals*. McGraw-Hill, New York (1953).
43. B. Chalmers, *Principles of Solidification*, Chapter 5. Wiley, New York (1964).
44. P. Duwez, R. H. Willens, W. Klement, Jr., *J. appl. Phys.* **31**, 1136 (1960).
45. R. Ray, Sc.D. Thesis, MIT, Cambridge, MA (1969).
46. R. Ray, B. C. Giessen and N. J. Grant, *Metall. Trans.* **3**, 627 (1972).
47. R. O. Elliott, A. M. Russell and B. C. Giessen, *J. mater. Sci.* **8**, 1325 (1973).
48. K. Togano and K. Tachikawa, Ref. [3], p. 519.
49. R. B. Russell, *Trans. AIME* **200**, 1045 (1954).
50. W. B. Pearson, *The Crystal Chemistry and Physics of Metals and Alloys*. Wiley-Interscience, New York (1972).
51. M. Hansen, *Constitution of Binary Alloys*, p. 723. McGraw Hill, New York (1958). See also Ref. [16], p. 438.
52. M. H. Cohen and D. Turnbull, *J. chem. Phys.* **31**, 1164 (1959); *Nature, London* **189**, 131 (1961).
53. D. Turnbull, *J. Phys. (Paris)*, Colloque-4, **35**, 1 (1974).
54. M. Marcus and D. Turnbull, Ref. [3], p. 211.
55. R. Ray, B. C. Giessen and N. J. Grant, *Scripta metall.* **2**, 357 (1968).
56. L. E. Tanner and R. Ray, unpublished results.
57. D. E. Polk, A. Calka and B. C. Giessen, *Acta metall.* **26**, 1097 (1978).
58. D. R. Uhlmann, *J. Non-Cryst. Solids* **7**, 337 (1972).
59. D. R. Uhlmann, *J. Non-Cryst. Solids* **25**, 43 (1977).
60. D. Turnbull, *Physics of Non-Crystalline Solids* (edited by J. A. Prins), p. 41. North-Holland, Amsterdam/Wiley-Interscience, New York (1965).
61. B. G. Lewis and H. A. Davies, *Liquid Metals* (edited by R. Evans and D. A. Greenwood), p. 274. Inst. of Physics, London (1976).
62. P. I. K. Onorato and D. R. Uhlmann, *J. Non-Cryst. Solids* **22**, 367 (1976).
63. P. G. Boswell and G. A. Chadwick, *Scripta metall.* **11**, 459 (1977).
64. L. C. Klein, C. A. Handwerker and D. R. Uhlmann, *J. Cryst. Growth* **42**, 47 (1977).
65. F. Spaepen, *Acta metall.* **23**, 729 (1975).
66. F. Spaepen and R. B. Meyer, *Scripta metall.* **10**, 257 (1976).
67. J. W. Christian, *The Theory of Phase Transformations in Metals and Alloys*, pp. 377-495. Pergamon Press, Oxford (1965).
68. J. D. Hoffman, *J. chem. Phys.* **29**, 1192 (1958).
69. D. Turnbull, *J. appl. Phys.* **21**, 1022 (1950).
70. L. Kaufman and H. Nesor, *Titanium Science and Technology* (edited by R. I. Jaffe and H. M. Burte), Vol. 2, p. 773. Plenum Press, New York (1973).
71. K. A. Jackson, *Solidification*, p. 121. ASM, Metals Park, OH (1971).
72. P. Ramachandrarao, B. Cantor and R. W. Cahn, *J. Non-Cryst. Solids* **24**, 109 (1977).
73. A. K. Doolittle, *J. appl. Phys.* **22**, 1471 (1955).
74. E. R. Bückle, *Nature, London* **186**, 875 (1960).
75. R. A. Grange and J. M. Kiefer, *Trans. ASM* **29**, 85 (1941).
76. J. H. Perepezko, D. H. Rasmussen, I. E. Anderson and C. R. Loper, Jr., *Proc. Int. Conf. on Solidification and Casting*, Sheffield (July 1977). To be published.
77. J. Schmidt and E. Hornbogen, *Z. Metallk.* **69**, 221 (1978).
78. F. Spaepen, Private communication.
79. P. G. Boswell and G. A. Chadwick, *Scripta metall.* **10**, 509 (1976).
80. J. L. Walter, S. F. Bartram and R. R. Russell, *Metall. Trans.* **9A**, 803 (1978).
81. U. Herold and U. Köster, *Rapidly Quenched Metals, III* (edited by B. Cantor), Vol. 1, p. 281. The Metals Society, London (1978).
82. L. E. Tanner, to be published.
83. P. G. Boswell and G. A. Chadwick, *J. mater. Sci.* **11**, 2287 (1976).
84. H. Warlimont, *Z. Metallk.* **69**, 212 (1978).
85. M. Naka, S. Tomizawa, T. Masumoto and T. Watanabe, Ref. [2], p. 73.
86. R. Ray, R. Hasegawa, C.-P. Chou and L. A. Davis, *Scripta metall.* **11**, 973 (1977).
87. B. G. Lewis and H. A. Davies, *The Structure of Non-Crystalline Materials* (edited by P. H. Gaskell), p. 89. Taylor and Francis, Cambridge (1977).
88. D. E. Polk and D. Turnbull, *Acta metall.* **20**, 493 (1972).
89. F. Spaepen and D. Turnbull, *Scripta metall.* **8**, 563 (1974).
90. J. J. Gilman, *J. appl. Phys.* **44**, 675 (1973).
91. H. S. Chen, J. T. Krause and E. Coleman, *J. Non-Cryst. Solids* **18**, 157 (1975).
92. H. S. Chen, *J. Non-Cryst. Solids* **22**, 135 (1976).
93. H. S. Chen, *Mat. Sci. Engng* **25**, 59 (1976).
94. H. S. Chen and J. T. Krause, *Scripta metall.* **11**, 761 (1977).
95. T. M. Hayes, J. W. Allen, J. Tauc, B. C. Giessen and J. J. Hauser, *Phys. Rev. Lett.* **40**, 1282 (1978).
96. J. J. Gilman, *Phil. Mag.* **B37**, 577 (1978).
97. D. S. Boudreaux, *Phys. Rev. B* **18**, 4039 (1978).
98. H. S. Chen, private communication (1978).